CHALMERS
UNIVERSITY OF TECHNOLOGY

Influence of piston cooling jet and renewable fuel blends on particulate emissions in a gasoline engine

Citation for the original published paper (version of record):
Muniappan, K., Dahlander, P., Helmantel, A. et al (2026). Influence of piston cooling jet and renewable fuel blends on particulate emissions in a gasoline engine. Fuel, 429. http://dx.doi.org/10.1016/j.fuel.2026.140897

Fuel 429 (2027) 140897

Contents lists available at ScienceDirect

Fuel

journal homepage: www.elsevier.com/locate/fuel

Full Length Article

Influence of piston cooling jet and renewable fuel blends on particulate emissions in a gasoline engine

M. Krishnamoorthi [a,*], Petter Dahlander [a], Ayolt Helmantel [b], Nika Alemahdi [b], Kalle Lehto [c]

[a] Chalmers University of Technology, 41296 Gothenburg, Sweden
[b] Aurobay 41755 Gothenburg, Sweden
[c] Neste Oyj, 02150 Espoo, Finland

ARTICLE INFO

Keywords:
GDI engine
Renewable gasoline
Piston cooling
Particulate emissions
Combustion images

ABSTRACT

Replacing a portion of the hydrocarbons in fossil fuels with renewable ones can lower net carbon dioxide (CO_2) emissions but may increase engine-out pollutants. Gasoline direct injection (GDI) engines emit particle number (PN) emissions due to fuel evaporation, mixing, and fuel composition issues. Piston cooling jets (PCJs) help reduce piston temperature but can decrease fuel evaporation. This study investigates PN emissions under PCJ-on and PCJ-off conditions at an indicated mean effective pressure (IMEP) of 9 bar, with varying start of injection (SOI) timing and fuel injection pressure (FIP). Images of combustion were captured to identify the sources of soot. Results indicate that the fuel film on the piston promotes pool fires and PN emissions under PCJ-on conditions. PCJ-off (hot piston) conditions showed ~ 99 % and ~ 35 % lower PN emissions than PCJ-on conditions at advanced and optimal SOI timing, respectively. Retarded SOI timing showed pool fires at the injector tip in both PCJ-on and PCJ-off cases. The effects of three gasoline blends (P, F1, F2) on PN emissions were investigated at 12–18 bar IMEP under hot piston conditions. Results indicate that all test fuels exhibited significant differences solely in particles with a mobility diameter of 10–100 nm. Particles with < 10 nm accounted for ~ 80 % of the total PN at higher IMEPs. Particles with 10–23 nm accounted for 52–75 % of particles larger than 10 nm. Hydrocarbon (HC) and nitrogen oxide (NO) emissions decreased, while PN and CO_2 emissions increased with increasing engine load.

1. Introduction

Gasoline direct injection (GDI) spark-ignition engines are widely used in light-duty vehicles. The global GDI market was $7.8 billion in 2023 and is expected to reach $14.2 billion by 2030 [1]. However, one of the challenges with GDI engines is minimizing engine-out volatile organic compounds and soot particles to reduce reliance on the gasoline particulate filter (GPF) and meet legal limits for particulate emissions. Gasoline consists of various hydrocarbons, such as paraffins, olefins, and aromatics, to achieve the desired fuel properties. Their concentrations in gasoline vary with fuel processing techniques and fuel standards. Different hydrocarbons exhibit distinct evaporation, combustion, and soot formation behaviors [2]. Paraffins and aromatics are the main components of gasoline, while olefins, naphthene, etc., are minor constituents [3].

Boosted GDI engines exhibit higher power density and combustion temperatures. Engine cooling is essential for maintaining optimal engine performance. Inefficient piston cooling raises the piston's temperature, potentially leading to mechanical failure. However, excessive piston cooling reduces fuel evaporation on the piston surface. GDI engines use aluminum pistons, and surface cooling proves sufficient. A piston cooling nozzle (PCN) at the bottom of the cylinder generates a lubricating oil jet, also known as a piston cooling jet (PCJ). The PCN oil flow rate is about 1.5–3 L per minute (lpm) [4]. The jet is directed onto the underside of the piston. PCJ is active when the oil pressure exceeds a threshold. On the other hand, solenoid-operated PCJs are managed by engine control units. Murthy et al. [5] reported that for gasoline engines, the PCJ is typically activated when the piston thermal load exceeds 0.45 kW/cm^2. Luff et al. [6] reported that switching off the oil jets increased piston temperature by up to 80 °C. They also noted that carbon monoxide (CO) emissions decreased by 5–10 % and fuel consumption (FC) by 1 % under low-speed, high-load conditions. Reduced piston temperature impedes fuel evaporation, leading to pool fires at some locations on the piston. The pool fires tremendously increase PN emissions. Targeting the PCJ oil jet on one side of the piston results in a ~ 50 K

* Corresponding author.
E-mail address: krishnamoorthism@gmail.com (M. Krishnamoorthi).

https://doi.org/10.1016/j.fuel.2026.140897
Received 6 April 2026; Received in revised form 19 July 2026; Accepted 5 August 2026

Nomenclature

Definitions Abbreviations

AMP	Accumulation mode particle
aTDC	after top dead center
bTDC	before top dead center
CAD	Crank angle degree
CA_{10}	The crank angle at 10 % of total heat release
CA_{50} or CP	Combustion phasing
CO	Carbon monoxide
COV	Coefficient of variation
CO2	Carbon dioxide
d_p, D_p	Mobility diameter
F1	Fuel 1 (Neste)
F2	Fuel 2 (Neste)
FC	Fuel consumption
FIP	Fuel injection pressure
GDI	Gasoline direct injection
GHG	Greenhouse gas
HC	Hydrocarbons
HRR	Heat release rate
IMEP	Indicated mean effective pressure
IVO	Intake valve open
NMP	Nucleation mode particle
NO	Nitrogen oxide
P	Fuel P (Preem 95E10)
PAHs	Polycyclic aromatic hydrocarbons
PCJ	Piston cooling jet
PCN	Piston cooling nozzle
P_{max}	Peak in-cylinder pressure
PM	Particulate matter
PN	Particle number
rpm	Revolution per minute
SOI	Start of injection
ST	Spark timing
Sub-10 nm	Particles smaller than 10 nm
Sub-23 nm	Particles smaller than 23 nm
VOC	Volatile organic compounds

temperature gradient across the piston [6]. Increasing the PCJ oil flow rate reduces the piston temperature, but the temperature gradient across the piston persists [7]. Excessive lubricating oil may be present on the liner during PCJ operation [8]. If the piston rings fail to contain the oil, it may form an oil film on the liner. Apicella et al. [9] reported that partial burning of the lubricant increased the number of sub-10 nm particles. Therefore, the impact of PCJ on/off on PN emissions from pool fires on the piston top and from lubricating oil on the liner needs to be examined.

Fuel injection pressure (FIP) and start of injection (SOI) timing are vital parameters for piston wall wetting and fuel–air mixing. An optical study by Yi et al. [10] revealed that 330° bTDC SOI showed higher yellow flames in the cylinder than 270° bTDC SOI. Yellow flames indicate the existence of hot soot particles. Zhang et al. [11] reported that increasing FIP with engine load helps reduce PN emissions. Jose et al. [12] reported that SOI of 310° bTDC resulted in improved fuel distribution, in-cylinder charge turbulence, and reduced wall wetting. Krishnamoorthi et al. [13 14] reported that 280° bTDC SOI timing showed lower PN emissions at medium engine loads. Therefore, optimal SOI and FIP reduce engine emissions; however, this also depends on fuel properties and engine conditions. Typically, gasoline is injected in sub-cooled spray conditions. Spray under sub-cooled conditions causes concentrated impacts on the piston and cylinder wall, resulting in strong shear forces. Flash-boiling spray conditions provide a widespread impinging area and dispersed momentum [15]. Increasing the fuel temperature can enhance spray distribution and fuel–air mixing under cold-start conditions, as reported by Nour et al. [16].

The fuel composition affects the engine-out particulate emissions. For instance, Abdellatief et al. [17] investigated the effects of renewable gasoline components on fuel properties and reported that isopropanol enhances the fuel's vapor pressure. Higher vapor pressure supports fuel vaporization and air–fuel mixing; however, very high vapor pressure can cause vapor lock and flash boiling. Low-vapor-pressure fuel with higher levels of unsaturated components increases PN emissions [18]. Replacing 7 % aromatics with bio-naphtha resulted in nearly the same PN but higher NOx emissions, as reported by Puricelli et al. [19]. Renewable naphtha, olefins, and ethyl *tert*-butyl ether (ETBE) components increase sub-23 nm particles. In contrast, Etikyala et al. [20] reported that adding 22 % ETBE to gasoline decreased sub-23 nm particles and increased $>$ 23 nm particles at 4.5 bar IMEP. The effect of fuel composition on PN emissions was low at low engine loads ($<$6 bar IMEP) [17]. At 9 bar IMEP, the ETBE blend showed higher $<$ 50 nm particles and lower $>$ 50 nm particles than gasoline [20]. This is caused by the rising engine load and speed, which impacts the air–fuel mixture. For instance, 10 bar BMEP (brake mean effective pressure) conditions showed 200 % higher PN than 4 bar BMEP, as reported by Ren et al. [21]. The fuel injection duration increases with engine load. Increasing FIP and advanced SOI timing help avoid fuel injections at late crank angles (later than 260°bTDC). Fuel injections at late crank angles reduce the time for mixing and evaporation. SOI at 230°bTDC showed 80 % higher PN than at 310°bTDC at 15 bar BMEP [22]. However, advanced SOI timing causes fuel wetting on the top of the piston, forming a fuel film. The evaporation of the fuel film depends on the piston temperature and fuel properties. Motoring the engine for a while with PCJ-on and engine transient conditions can lower the piston temperature. Therefore, advanced SOI timing under PCJ-on conditions increases PN emissions. Five seconds of motoring increased PN by 4-times for a while due to pool fires on the piston and injector tip [13]. Advanced SOI timing with PC-off enhances fuel film evaporation and mixing. Under these conditions, PN formation depends on fuel–air mixing and fuel chemistry rather than on pool fires in the cylinder. Reports on how gasoline composition affects PN emissions under high-load, hot-piston conditions are limited.

The study includes two testing campaigns. The first investigates how toggling PCJ on and off affects PN emissions at medium engine loads due to fuel wall-wetting-derived pool fires in modern GDI combustion systems. Second, it investigates how gasoline formulation impacts PN emissions at high engine loads under no-pool-fire-like conditions. This study helps reduce tailpipe emissions in relation to the European Union's 2035 CO_2 emissions target. Modern GDI engines continue to be used in plug-in hybrid electric vehicles. Understanding soot formation from pool fires and diffusion combustion remains highly relevant to reducing PN emissions from combustion engines.

2. Experimental methods

2.1. Engine setup and instruments

A single-cylinder research engine testbed (AVL Puma 5411) was used in this study [23]. The piston and cylinder head mimic the geometry of a production-version light-duty spark-ignition GDI engine. The engine features two intake and two exhaust valves, dual camshafts, and lash adjusters. The technical specifications of the test engine and the setup are shown in Table 1 and depicted in Fig. 1. Moisture-free compressed air was used to boost the intake. The fuel injection system consisted of a fuel measuring unit (AVL 733 s), a Denso high-pressure pump (HP3), a common rail, an injector, and an electronic control unit (ECU). A National Instruments (cRIO9411) direct injection driver kit was used to

Table 1
Technical specifications of the test engine.

Parameter	Values
Bore/ stroke (mm)	82.4/90
Connecting rod length (mm)	139.5
Compression ratio	11.6:1
Tumble ratio	1.7
Valve actuation	Roller follower and hydraulic lash adjuster
Boosting system	External supply, 02 bar gauge
Injector	Inward opening, spray-guided, 100–700 bar FIP, 12.5 cc n-heptane at 100 bar FIP

control the fuel injector. The fuel injector had six holes, and the spray plumes were not symmetrical. An air preheater, throttle controller, AVL 733 s, injection driver, and ignition system were interfaced with AVL Puma. The ignition system can deliver up to 100 mJ to the spark plug. TTL (transistor-transistor logic) signals controlled the ignition coil, injector, and camera.

A Kistler pressure sensor (model 6045B) and an AVL 365 crank angle encoder were used to measure in-cylinder pressure data. An AVL Indicom data acquisition system enables online monitoring of all combustion data, including IMEP and combustion phasing (CA_{50}). Gaseous emissions were measured using three instruments on the emission rack. The flame ionization detector measures HC emissions (C1 equivalent), the Chemiluminescence detector measures NOx emissions, and the nondispersive infrared detector measures CO and CO_2 emissions. The gas sample was maintained at 190 °C to avoid hydrocarbon condensation. Gaseous emissions were measured for 30 s per test, and the average value was recorded in the AVL Puma. A Horiba Mexa 110 was used to measure the exhaust-gas lambda. Cambustion DMS500 MkII fast particle analyzer measured particle number and size concentrations in the exhaust gas. The engine exhaust gas pressure and temperature exceeded the DMS500 limits. Hence, an air-to-gas double-pipe heat exchanger and restrictor washer were used to maintain the sample gas temperature (~150 °C) and flow rate (~8 lpm). Particles were sampled for 5 min at 2 Hz per test. The primary dilution ratio was 5:1 (for gasoline engines), and the secondary dilution ratio was adjusted based on the particle concentration in the exhaust gas. The DMS500 measures the particles from 5 nm to 1000 nm. The DMS500 works well when the PN concentration exceeds the threshold. The PN measurement threshold of the DMS500 varies with particle size. The threshold count for DMS500 is 2.5e4 #/cc for a 10 nm particle size, and 180 #/cc for a 1000 nm particle size. A catalytic stripper or volatile particle remover was not used to remove volatile particles from the exhaust gas samples. Hence, DMS500 measures all particles in the sample. The volatile particle count increases as the exhaust gas sample temperature decreases due to condensation of heavy hydrocarbons.

2.2. Fuels

All three test fuels met the EN 228 standard. Fuel 1 (P) was a commercial gasoline 95E10S (made by Preem AB, Sweden). Fuels 2 and 3 (F1 and F2) were non-commercial fuels (made by Neste Oyj, Finland) used in this study. The physicochemical properties of test fuels are given in Table 2. Replacing certain fuel hydrocarbons without altering other hydrocarbons in the fuel or the fuel's distillation properties is challenging. Hence, the test fuel's composition and distillation properties

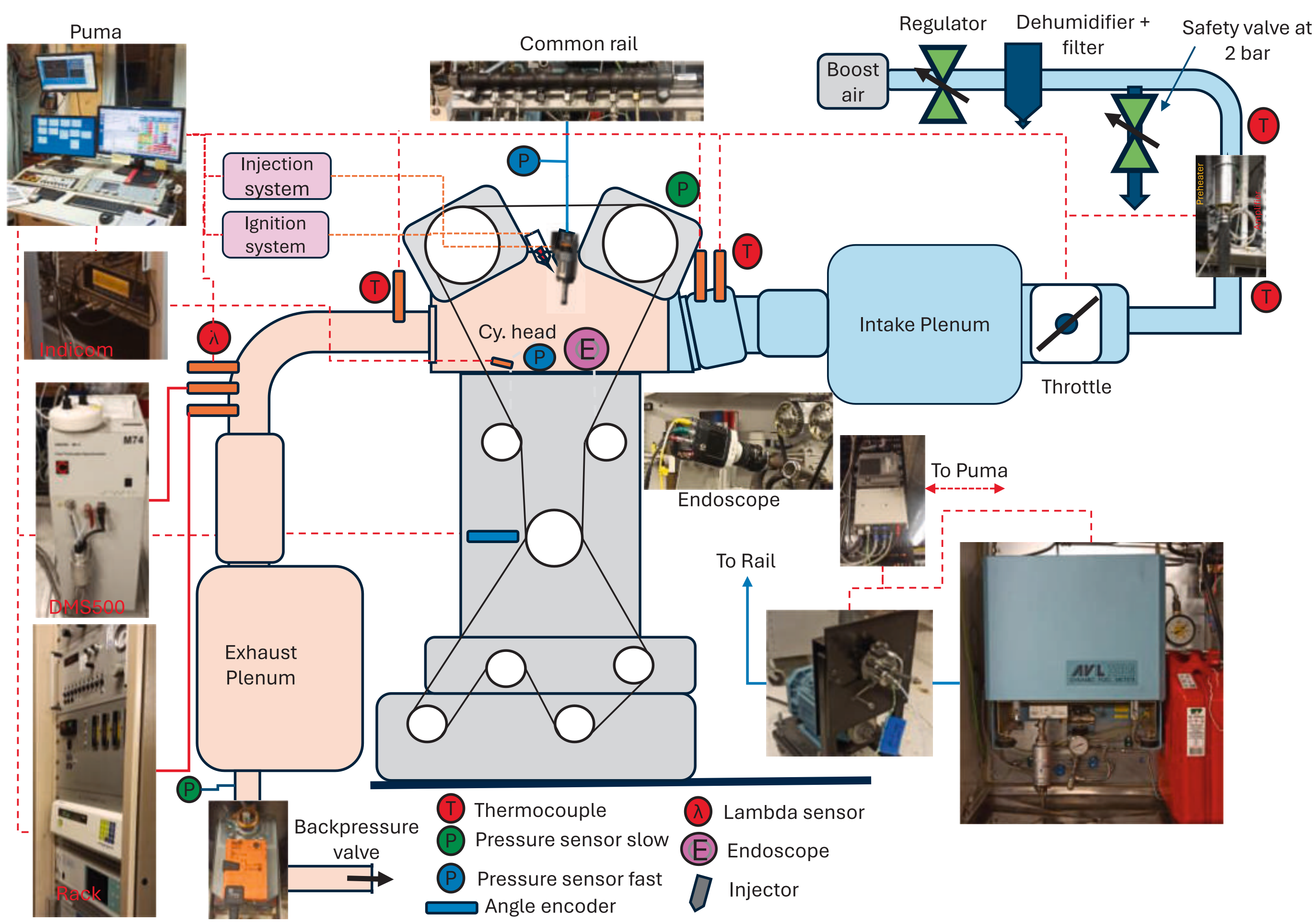

Fig. 1. Schematic diagram of the test setup for gasoline blend combustion.

Table 2
Properties of the test fuels.

Property	Test methods	P	F1	F2
Density (kg/m^3)	EN ISO 12185	747.6	742.0	738.2
Sulfur (mg/kg)	EN ISO 20846	<3.0	2.2	7.4
Initial boiling point, IBP, (°C)	EN ISO 3405	35.8	34.5	38.6
T10 (10 % v/v evap.), (°C)	EN ISO 3405	54.5	51.8	55.4
T50 (50 % v/v evap.), (°C)	EN ISO 3405	91.2	78.1	79.0
T60 (60 % v/v evap.), (°C)	EN ISO 3405	108.4	105.3	99.9
T90 (90 % v/v evap.), (°C)	EN ISO 3405	146.4	148.2	148.4
Final boiling point, FBP, (°C)	EN ISO 3405	182.9	183.6	186.6
Lower heating value (MJ/kg)	ASTM D240	41.38	41.64	41.80
Vapor pressure (kPa)	EN 13016–1	57.9	57.7	51.4
Benzene (% v/v)	EN ISO 22854	0.51	0.39	0.44
Olefins (% v/v)	EN ISO 22854	8.4	2.1	6.1
Naphthene (vol. %)	EN ISO 22854	12.1	8.6	7.0
Iso-paraffins (vol. %)	EN ISO 22855	45.6	44.1	46.2
N-paraffins (vol. %)	EN ISO 22855		9.4	8.9
Aromatics (% v/v)	EN ISO 22854	23.9	26.4	21.9
C9+ Aromatic (% m/m)	EN ISO 22855	7.6	9.72	9.27
C10+ Aromatic (% m/m)	EN ISO 22856	0.7	1.05	1.28
Ethanol content (% v/v)	EN ISO 22854	9.85	9.11	9.63
RON	EN ISO 5164	>95.0	>95.4	>95.7
MON	EN ISO 5163	>85.0	>87.4	>87.3

differed, and their combined effect on PN was analyzed. F2 contained more renewable components, which could lower GHG emissions by 9 % compared to the fossil gasoline comparator (94 g CO_2e/MJ). Meanwhile, P and F1 reduce GHG emissions by 4 %. IBP-T50 plays a vital role in emissions during cold start and low load. T60-FBP influences fuel evaporation at high engine loads. Olefins were higher in P than in the other fuels. F1 contains a higher proportion of aromatics than the other two fuels. Heavy aromatic hydrocarbons could increase soot emissions.

2.3. Experimental test conditions

Two test campaigns used different engine setup conditions. An endoscope was used in Campaign 1, whereas a metal plug was used in Campaign 2 (Fig. 2). Hence, combustion images were not captured during test Campaign 2. A PCN was used in Campaign 1 but not in Campaign 2. Intake valve opening and closing timings were 337 and 484°aTDC, respectively; similarly, for exhaust valves, 173 and 356°aTDC. The valve open and close timings are measured at a standardized 1 mm lift point. The piston top ring gap was about 0.5 mm when fitted in the cylinder. The coolant and lubricating oil (5 W-40) temperatures were maintained at ~ 90 °C.

The tests were conducted at an IMEP of 09–18 bar and 2000 rpm, corresponding to approximately 40–80 % engine load for the 145-kW production engine [24]. GDI engines typically work at higher engine speeds (1500–4500 rpm). The operating condition of 9-bar IMEP was selected to represent a medium-load condition commonly encountered in practical engine operation, and 2000 rpm was selected to minimize cycle-to-cycle variability and experimental uncertainty. The production engine operates without piston cooling up to 9 bar IMEP at 2000 rpm. Hence, the tests were conducted at 9 bar IMEP under both PCJ-on and PCJ-off conditions. SOI and FIP were varied during Campaign 1. The engine was operated under stoichiometric conditions during the study. The exhaust-gas lambda was 1 ± 0.001 in both test campaigns. The coefficient of variation of IMEP (COV_{IMEP}) was less than 0.6 % at 9 bar IMEP, and it rose to 1.6 % at 18 bar IMEP.

The boost, FIP, and back pressure increased with engine load, as shown in Table 3 (based on pre-study). Campaign 2 (12–18 bar IMEP) used advanced SOI timing and higher FIP to reduce injector tip wetting and improve air–fuel mixing. The engine timing unit (ETU) controlled the SOI and spark timings. The engine operations above 11 bar IMEP at 2000 rpm are in a knock-limited region [14]. In this region, the maximum brake torque condition, corresponding to the 50 % total heat release (CA_{50}) position, is delayed, thereby preventing excessive in-cylinder pressure and knocking. Knocking was observed during preliminary tests with retarded CA_{50} (see Appendix) due to the gas exchange process. However, no knock was observed during the tests.

2.4. Piston cooling nozzle and imaging

Fig. 2(a) shows the PCN and oil jet target. The oil jet was turned on and off using an in-house-built setup. PCN provides an oil flow rate of 2.3 L per minute (lpm). The oil jet hits the underside of the piston. A Lavision hybrid UV camera endoscope was mounted on the cylinder head to capture combustion images. A Phantom Miro M310 high-speed color camera and a Carl Zeiss 85 mm lens were used. More details on the engine, endoscope, and camera setup can be found in Refs. [13,14]. The camera view of the combustion chamber, illuminated by an external light source, is shown in Fig. 2(b). It shows a J-gap spark plug and piston at a 30°aTDC crank position. No external light source was used during the measurement. Phantom camera control software with default RGB values was used in this work. The camera software system was 12-bit; therefore, the image with 4096 pixels was saturated. The combustion image should have a pixel value less than 4096 to observe variations within the image. The same camera settings were used for all tests. RGB color details were in the image. Images were acquired at 512x484 pixel resolution with an exposure time of 18.4 μs. The combustion images were captured at crank angle degree (CAD) from −15° to 57° (1 image/CAD) over 100 combustion cycles to obtain statistical results. The high-speed color camera detects visible wavelengths, usually from 400 to 700 nm. In this study, the main signal comes from blackbody radiation emitted by hot soot. At these settings, blue flames are less visible, but this does not affect soot detection because soot is closely linked to

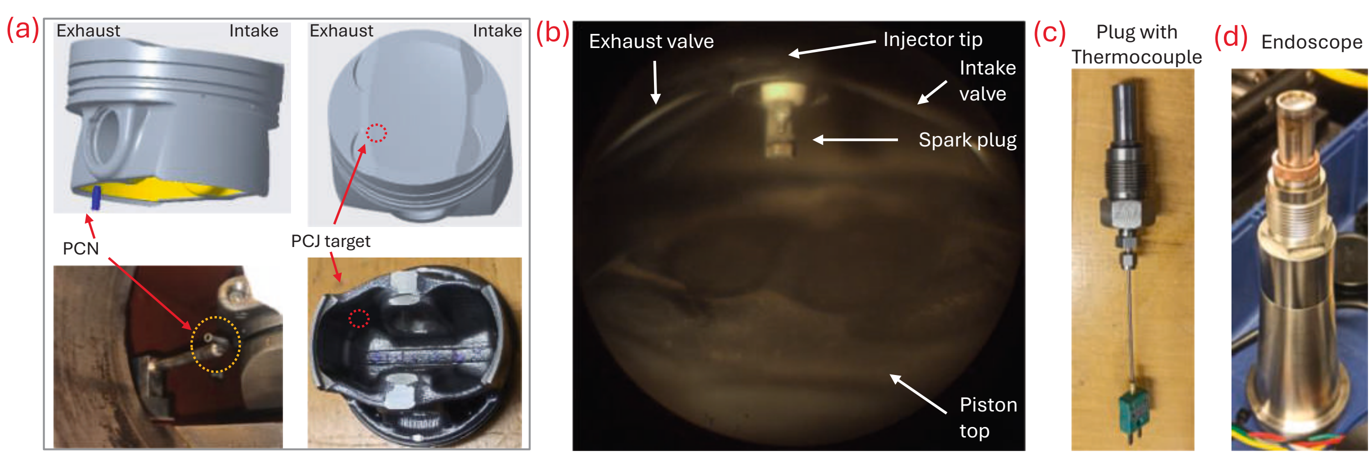

Fig. 2. (a) PCN and piston arrangement, (b) Camera view of the combustion chamber, (c) metal plug, and (d) an endoscope.

Table 3
Engine operating conditions during load variation and PCJ studies.

IMEP (bar)	Intake pressure (mbar)	Intake Temperature (°C)	Back pressure (mbar)	FIP (bar)	SOI timing (°bTDC)	CA_{50} (°aTDC)	Test
09	920	27	1020	300, 400	330–260	08.0	Campaign 1
12	1123	27	1120	400	325	13.0	Campaign 2
14	1326	27	1250	425	330	18.0	
16	1544	28	1350	435	340	22.0	
18	1765	29	1500	450	340	24.0	

blackbody radiation, which appears as a yellow, luminous flame.

In-house MATLAB scripts were used to post-process combustion images and extract statistical data. The yellow flames in the images were identified by thresholding the red channel of the RGB images [25]. This method works well when the image shows a distinct contrast between flame and non-flame areas. The same threshold value was applied to all images. The images were binarized using an appropriate threshold, and the resulting binary images were then used to generate spatially resolved relative-frequency (RF) images. An RF of 1 means the yellow flame appears in every image at a specific crank angle, enabling qualitative analysis of the data across 100 combustion cycles. The RF images were overlaid on a gray, illuminated background to show the statistical positions of the yellow flames in the combustion chamber.

2.5. Measurements and uncertainty

The engine started and ran for 30 min to reach a steady-state engine condition, after which the measurement campaign began. All measurements were taken under steady-state engine conditions, and the engine remained in continuous firing mode during the test. The COV_{IMEP} was less than 2 % under steady-state conditions. The engine ran for a certain time at each test point before the measurement. Hence, PN and gaseous emissions measurements were taken under steady-state conditions for 5 min, which included cycle-to-cycle variations, and PN were repeatable [14]. During this 5-minute period, 100 combustion-cycle images were captured and used in RF calculations. The combustion images showed acceptable repeatability. The average 5-minute PN data, along with one standard deviation (SD), was used in the discussion. The SD of PN was higher when PN was below DMS500′s threshold limit. Changing the test order and retesting on another day led to small changes in PN emissions. The engine should run for a set duration at each test point to obtain stable, repeatable PN results. The retest experiments were performed to observe the repeatability of PN results. About 70 % repeatability was observed in the PN data.

2.6. Energy analysis

The energy analysis helps explain how the fuel energy is distributed within the engine [26]. In engines, the input fuel energy is converted into useful power, heat losses, and unburned fuel losses.

Input fuel energy = work net + pumping losses + combustion losses + exhaust gas energy losses + in-cylinder energy losses.

Input fuel energy (E_f) = mass flow rate of fuel ($\dot{m}_f$) × lower heating value of the fuel (.LHV_f)

Work net = IMEP × displacement volume (V_{disp}) × engine speed (rpm) / (60 × 2 × E_f).

Pumping losses = gross IMEP – net IMEP.

Combustion inefficiency $=.\frac{m_{co}LHV_{co}+m_{hc}LHV_{hc}}{E_f}$

Exhaust energy losses = mass of exhaust gas (m_{eg})× specific heat of exhaust gases (C_{eg}) × (Exhaust gas temperature – ambient temperature) $/.E_f$

Calculating combustion inefficiency using HC and CO species in the exhaust gas is a simplified approach. However, including combustion products such as hydrogen and aldehydes, as well as particulate matter, in the energy calculation would provide a complete view of the energy analysis.

2.7. Particulate (particle) formations and analysis

Fuel impingement on the combustion chamber walls results in liquid fuel films, fuel-rich regions in the cylinder, and a lack of air–fuel homogenization. When combustion begins, the fuel-rich regions are exposed to high temperatures, leading to incomplete combustion and fuel pyrolysis. Under pyrolysis-like conditions, carbon-rich fuel molecules produce soot precursors such as small PAHs [27]. The soot formation process is complex, involving gas-phase chemistry and particle dynamics. Small PAHs grow into bigger PAHs in high-temperature regions in the hydrogen abstraction carbon addition (HACA) pathway [28]. Gas-phase PAHs form solid particles or coagulate with other PAHs, depending on their size [29]. The soot particles then agglomerate and coagulate, forming larger particles. In addition to solid soot particles, incomplete combustion produces volatile particles. Particles are classified as solid soot if they remain solid above 300 °C, whereas volatile particles become vapor. The counts of volatile particles increase as sampling temperature decreases due to condensation.

Paraffins, naphthene, and olefins produce fewer soot precursors than aromatics. Unsaturated fuel molecules (aromatics and olefins) form more soot precursors than saturated ones (paraffins). Sooting tendency decreases in the order of aromatics, naphthenes, olefins, and paraffins. The sooting tendency increases with the equivalence ratio, and the rate of increase is significantly more for aromatics than for paraffins. Heavy aromatics (C9+) contribute more to soot emissions, and their tendency to form soot increases with engine load. Ethanol has less impact on soot precursor formation compared to paraffins, and its OH radicals oxidize soot precursors. More details on fuel composition and its effect on soot formation can be found in Refs. [13,14].

Incomplete combustion also produces volatile organic compounds (VOCs), heavy hydrocarbons, and other substances that nucleate, forming semi-volatile organic compounds (SVOCs). C6-C8 aromatics (toluene, benzene, etc.) yield more SVOCs [30]. SVOCs can form volatile particles or condense on solid particles. In the latter case, the volatiles-to-solid-particle ratio affects particle size. Semi-volatile PAHs collide and cluster, resulting in gas-phase into liquid-like nano-droplets. The intermediate species are active precursors responsible for soot inception rather than passive indicators of its presence. SVOCs also undergo dehydrogenization, forming soot particles.

Clustering of soot particles increases particle size. Hence, particle formation via various chemical and physical interactions can distort measurements and introduce uncertainty into PN data. Additionally, cyclic variations in FIP, fuel–air mixture, and combustion influence particle formation. It is hypothesized that most volatile particles exist in the nucleation mode (sub-23 nm, $d_p < 23$ nm), whereas most solid particles exist in the accumulation mode ($d_p > 23$ nm). Some solid soot particles and metallic elements are in the sub-23 nm group. Hence, the exhaust gas contains both volatile and solid soot particles.

3. Results and discussion

3.1. Campaign 1: PCJ studies

The effects of PCJ on combustion, PN, and gaseous emissions were analyzed using fuel P. In-cylinder pressure and heat release rate (HRR) at different FIP and SOI timings are shown in Fig. 3. The HRR trend was almost identical for SOI timings, except for the 270 SOI. The maximum HRR was observed between 60 and 75 J/CAD. A slightly higher in-cylinder pressure was observed at 270 SOI due to slightly earlier CA_{50}. The minimum and maximum cylinder pressures ranged from 45 to 56 bar due to cyclic variations. CA_{50} lies between 8 and 9°aTDC for the test cases. The 10 % total heat release (CA_{10}) was observed slightly later (0.3 to 0.8 CAD) in PCJ-on cases compared to PCJ-off cases. Meanwhile, CA_{90} was delayed by 0.7–1.43 CAD in PCJ-on cases compared with PCJ-off cases. Hence, a slightly shorter combustion duration was observed in the PCJ-off than in the PCJ-on cases. SOI timing of 270 showed a slightly earlier CA_{90} than the 330 SOI timing cases, possibly due to improved spray-air interaction. Hence, 270 SOI showed higher thermal efficiency than 330 SOI in PCJ-on cases (Fig. 5). The in-cylinder pressure rise rate was slightly higher (0.7 bar) for retarded SOI than for advanced SOI cases. PCJ-off and PCJ-on cases exhibited nearly identical combustion characteristics at a typical SOI timing. Likewise, 400- and 300-bar FIPs showed similar combustion characteristics.

Variations in CA_{10} and CA_{90} for PCJ on– and off-cases are shown in Fig. 4. At advanced SOI timings, PCJ-on cases showed slightly later CA_{10} than PCJ-off cases. This could be due to a slightly colder charge near the spark plug, given a tumble motion [14]. Spark timing was slightly adjusted for the test cases to achieve the desired CA_{50}. It was 12° and 11.5° bTDC for the PCJ-on and PCJ-off cases across all SOI cases except 270 SOI. For 270 SOI, spark timing was 1 CAD later than for the other SOI cases. Retarded SOI timings showed delayed CA_{10} due to changes in fuel–air mixing. Pool fires occur during the late combustion cycle in PCJ-on cases, increasing CA_{90} relative to PCJ-off cases. The CA_{10} and CA_{90} were nearly the same for test cases at 290 SOI timing. 270 SOI showed earlier CA_{90} than other SOIs, possibly due to a stratified charge closer to the spark plug. The stratified charge could result in higher PN (Fig. 7). At 300 bar FIP, 270 SOI showed higher PN than 300–260 SOI cases (400 bar FIP also shows this trend) However, the PM was nearly the same for 290–260 SOI cases (Fig. 8).

3.1.1. *Energy analysis*

Fig. 5 shows the different forms of energy conversion for the PCJ-on and PCJ-off cases. The useful energy conversion and the losses are specified as percentages of the input fuel energy.

During the test, the input fuel energy was adjusted to maintain a constant IMEP. The PCJ-off cases showed slightly higher (0.3–1.1 %) work output than PCJ-on cases. A higher cylinder boundary temperature during PCJ-off helps reduce HC and CO emissions. Hence, PCJ-off cases showed slightly lower combustion inefficiency (0.5 %) and in-cylinder losses (0.2 %) than the PCJ-on cases. The COV_{IMEP} was up to 9 % and 4 % higher for the 330 and 260 SOI cases, respectively, under PCJ-on than under PCJ-off, except at optimal SOI timings, where the values were nearly the same. The FIP fluctuated by 20 bar under steady-state engine tests, resulting in variations in COV_{IMEP} [13]. Pumping losses were nearly similar for the PCJ on/off cases. The exhaust heat losses were slightly lower in the PCJ-on than in the PCJ-off cases at 290–260 SOI timings. This indicates that the in-cylinder charge temperature was slightly higher in PCJ-off cases. Improved fuel evaporation and higher cylinder temperature help reduce soot emissions. In-cylinder combustion losses (unaccounted losses) were almost similar for PCJ-on and PCJ-off cases. Hence, the slightly higher work output during the PCJ-off condition was due to lower combustion inefficiency. Compared with 400-bar FIP, 300-bar FIP reduces fuel atomization and evaporation, resulting in higher combustion inefficiency.

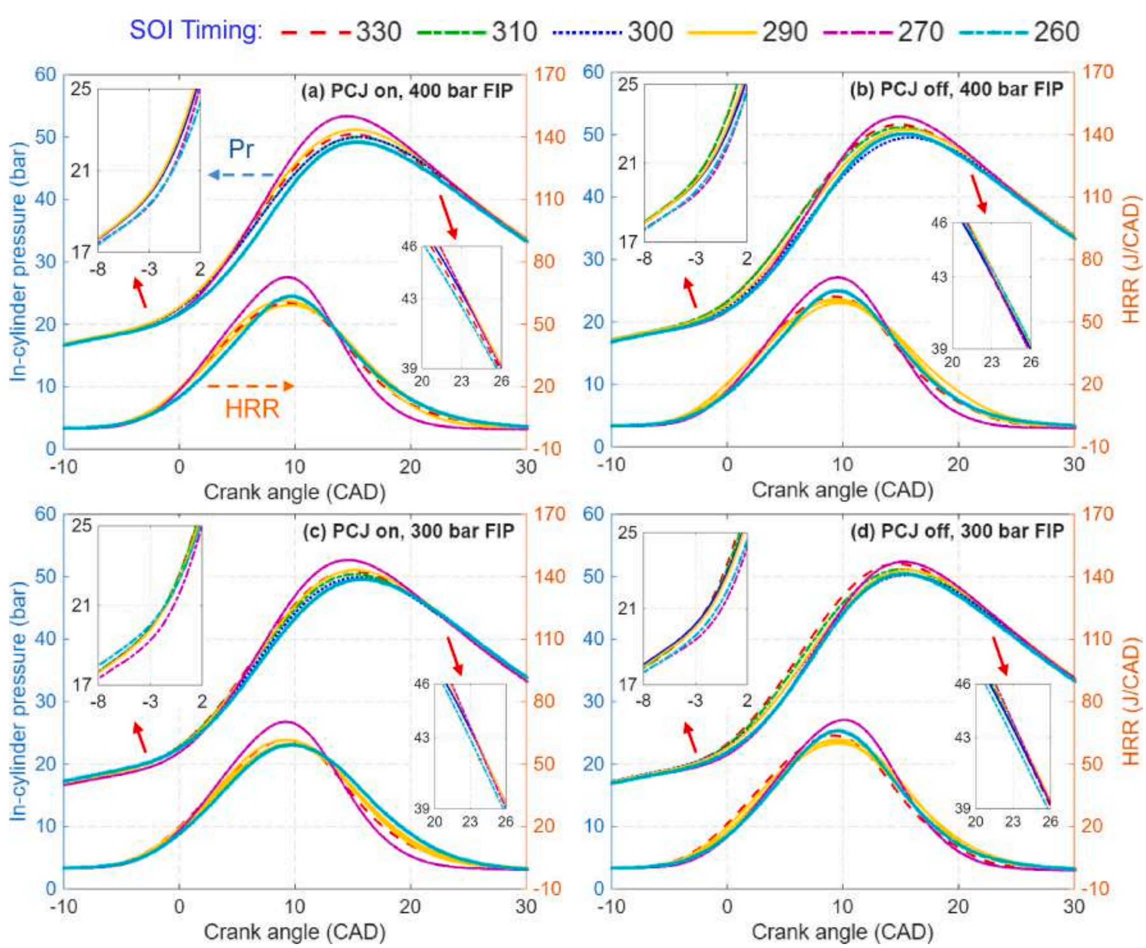

Fig. 3. In-cylinder pressure and HRR at SOI timings for PCJ on/off cases.

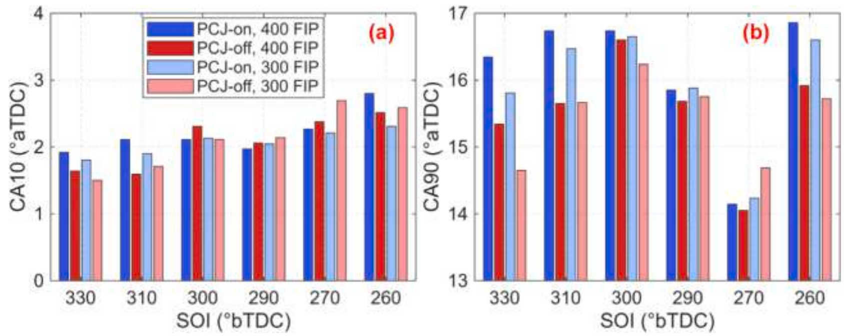

Fig. 4. CA_{10} and CA_{90} for PCJ on– and off-cases at 400 and 300 FIPs.

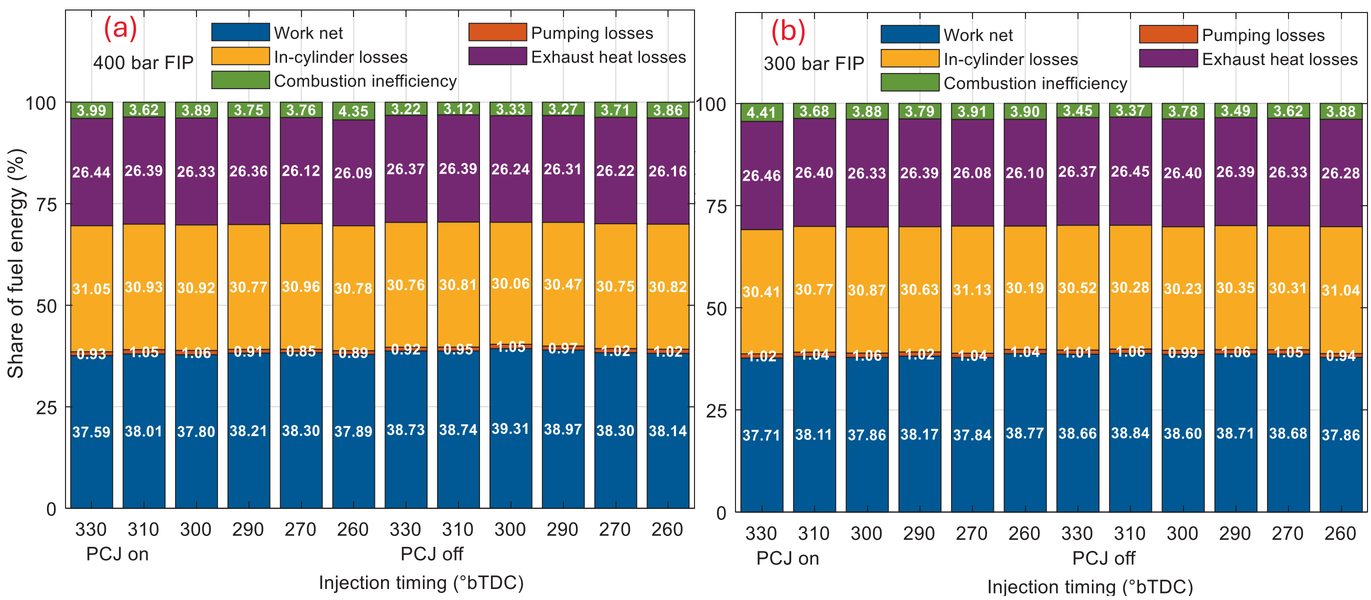

Fig. 5. Energy share analysis for various SOI timings at 400 bar FIP (left) and 300 bar FIP (right).

3.1.2. Particulate emissions

The particle number concentration (PNC) from 5-minute data is shown in Fig. 6. The PN data were stable, and the standard deviation was very low. This indicates that the cycle-to-cycle variations effect on PN were very low ($COV_{IMEP} < 0.7$ %). A significant variation in standard deviation was observed for particles > 200 nm, but they were less numerous. Advanced SOI timing directs more fuel to the piston top, leading to wall wetting (and fuel film), whereas retarded SOI timing creates fuel-rich pockets in the bulk mixture due to a shorter fuel evaporation time. 330 SOI showed higher PNC than retarded SOI timing when the PCJ was on. The piston temperature was lower when the PCJ was active, creating a temperature gradient across the piston [7]. Lowering piston temperature slows the evaporation of the fuel film, leading to pool fires on the piston top, as shown in Fig. 9. Pool fires produce soot that deposits on the piston. The soot buildup on the piston then absorbs fuel, leading to more pool fires. The formation and breakup of these deposits depend on the liquid fuel film. Advanced SOI timing showed two PN size ranges, which may come from different sources. The pool fires on the piston could produce < 300 nm particles, whereas the breakdown of soot deposits seems to yield 500–1000 nm particles. Wang et al. [31] reported that 330 SOI showed more 23–800 nm particles, whereas 180 SOI showed more < 23 nm particles. They also reported that > 200 nm particles were nearly identical for SOI timings later than 300°bTDC.

When the PCJ was off, the hotter piston facilitated fuel evaporation and reduced pool fires on the piston. Therefore, particles at 330 SOI timing were lower than at retarded SOI timing. SOI timing between 300 and 260 showed only a slight difference in PNC. These SOI timings reduce fuel impingement on the piston. The intake valve lift peaked at 307° bTDC, and airflow was likely higher during this period. Slight variations in air–fuel interactions lead to slight variations in PNC [32]. Sub-23 nm and greater than 200 nm particles showed sensitivity to SOI timing in PCJ-on cases. In PCJ-off cases, differences in PN for SOI cases were observed mainly for 50–200 nm particles. This may result from fuel-rich zones in the bulk mixture. Krishnamoorthi et al. [13] observed that 290–260 SOI timings affect 23–200 nm particles more, and that pool fires increase > 23 nm particles, whereas diffusion flames in the bulk increase sub-23 nm particles. As with the 400 bar FIP and PCJ-on cases, the PNC observed at SOI timings (300-260°bTDC) did not vary significantly for 300 bar FIP cases, especially for particles smaller than 300 nm. The 300 bar FIP cases showed a fuel injection duration about 15 % longer than at 400 bar FIP. Lower FIP may produce larger fuel droplets that are less affected by air turbulence. Therefore, fuel–air mixing appears to be governed more by thermal evaporation than by turbulence mixing, compared to 400 bar FIP.

Different PN size groups with respect to SOI timing are shown in Fig. 7. At 330 SOI timing, PCJ-on cases showed 100–140 and 15–20 times higher > 10 nm and sub-10 nm particles, respectively, than PCJ-off cases. However, >10 nm PN was only 33–52 % higher for PCJ-on than PCJ-off at 300 SOI due to less fuel impingement on the piston. Pool fires on the piston seem to increase all particle sizes but greatly increase those in the > 10 nm range. The consequences of piston cooling

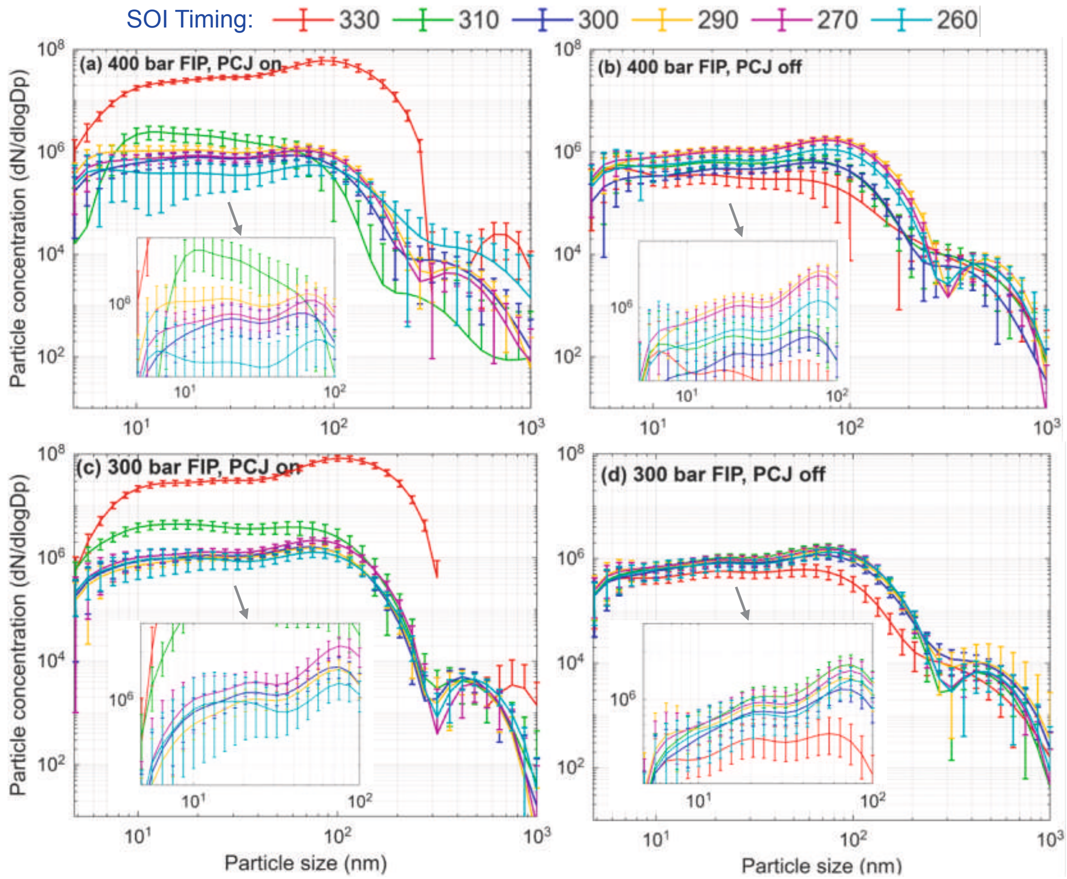

Fig. 6. SOI timing effects on particle emissions under PCJ on/off conditions.

on PN emissions were less pronounced under retarded SOI timing, as fewer fuel parcels reached the piston (no visible pool fires on the piston). 260 SOI could have a shorter mixing time, resulting in diffusion flames in the bulk that moderately affect > 200 nm particles. Retarded SOI cases showed pool fires at the injector tip, as shown in Fig. 9. Pool fires at the injector tip affect > 10 nm particles more. At 400 bar FIP, retarded SOI timing (290–260 SOI) resulted in 22–45 % higher > 10 nm particles in PCJ-off cases compared to PCJ-on cases. The reason for this increase in PN is unclear. Moreover, no significant differences in the yellow flames were observed in these cases (Fig. 10).

PCJ-on cases could increase fuel impingement on the liner (fuel–oil film), thereby increasing sub-10 nm particles [8]. At 300–260 SOI timings, most PCJ-on cases showed slightly more or less (±35 %) sub-10 nm particles than PCJ-off cases. During SOI variations, sub-10 nm particles showed < 35 % change between SOIs in PCJ-off cases. Hence, the amount of oil film on the liner was not significantly increased by the PCJ. Under PCJ-on conditions, 330 and 310 SOI showed up to 14-times higher sub-10 nm particles than 300 SOI cases. This indicates that pool fires on the piston increase sub-10 nm particles.

For most SOI timings, PN was significantly higher at 300 bar FIP cases than at 400 bar FIP cases. Decreasing FIP could increase fuel-droplet size, thereby reducing fuel–air mixing. On the other hand, the 300-bar FIP cases could reduce wall wetting and piston pool fires for advanced SOI cases, as shown in Fig. 9. Air-fuel mixing is the primary factor influencing PN emissions rather than wall impingement in retarded SOI cases. Lowering FIP increases fuel injection duration, thereby increasing the mass of liquid fuel parcels at the start of combustion. These fuel parcels undergo diffusion combustion, increasing PN. Hence, 300 bar FIP and retarded SOI timings yielded more > 23 nm particles than 400 bar FIP cases. Overall, 300 SOI showed nearly identical PN emissions for the PCJ-on and PCJ-off cases and lower PN emissions than at other SOI timings.

When the PCJ was turned on, PN emissions increased. The PN count stabilized after 15 min; the total PN increased by 270-fold (330 SOI). This indicates that the PCJ initially cools the piston, which promotes deposit formation. Eventually, the deposits reach saturation. When the PCJ was turned off, PN decreased and stabilized within 5 min. At that time, the total PN was 100 % higher than the initial PCJ-off level; afterward, it gradually decreased. Therefore, it is concluded that the PN did not return to the original PCJ-off level, at least within 5 min. The piston temperature increases with engine load, which promotes fuel evaporation. A longer fuel-injection duration at high loads results in local fuel-rich regions within the cylinder. Hence, tests were conducted at IMEPs of 12 and 14 bar, with variations in SOI timing (section 3.1.7).

Particulate matter (PM) mass was calculated from PN and density (1000 kg/m^3), assuming spherical particles. Pool fires on the piston case showed very high PM emissions. At 310 and 300 SOI cases, 400 bar FIP showed 25–85 % lower PM than 300 bar FIP (Fig. 8). This indicates 300 bar FIP forms larger particles. 290–260 SOI cases did show similar PM.

3.1.3. Combustion images

Random-cycle combustion images for the PCJ-on and PCJ-off cases are shown in Fig. 9. The random-cycle combustion images show one of the 100 combustion-cycle images, helping to see the yellow flames. However, their intensity and location vary with combustion cycles (Fig. A2). A bright yellow flame indicates hot soot, leading to particle emissions [33]. Yellow fires observed on the piston and at the injector tip are ‘pool fires.’ Yellow fires in the bulk of the cylinder are diffusion flames. Sun et al. [34] reported that the total flame intensity peaked after the crank angle corresponding to the maximum HRR (~8°) and then decreased as the piston descended. PCJ-on cases showed luminous flame on the piston top, indicating pool fires from the fuel film. Singh

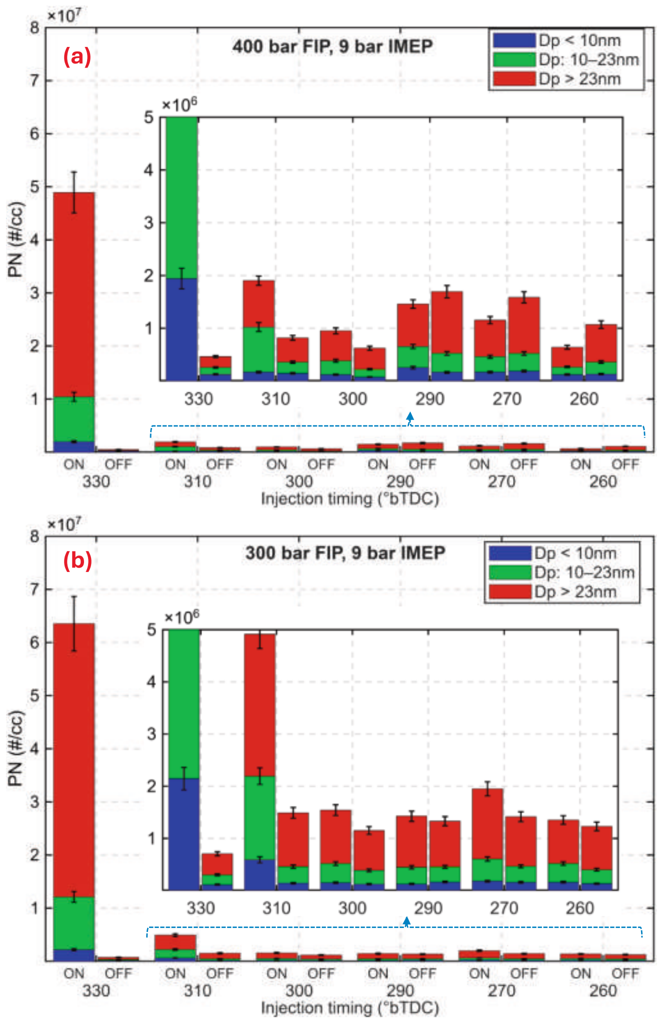

Fig. 7. PN at different SOI timings in PCJ on/off at 400 bar FIP (a) and 300 bar FIP (b). Sub-10 nm (blue), 10–23 nm (green), and > 23 nm (red) particles.

et al. [35] reported that diffusive combustion (pool fires) on the piston top was characterized by a yellow flame due to soot luminosity. They observed a larger time delay between the flame passing over the fuel film and the formation of soot. The pool fires were observed until the 57°aTDC (last frame). Pool fires on the piston last longer than those on the injector tip, and they have different intensities [34]. The fuel that burns after primary combustion (CA_{90}) contributes more to PN emissions. Unlike 330 SOI, yellow flames on top of the piston were not observed at SOI timings of 300 or later. Because the advanced (330) SOI cases form a thicker fuel film than retarded SOI cases. The heat from the piston vaporizes the small fuel film formed by retarded SOI cases. Nevertheless, retarded SOI timing resulted in pool fires at the injector tip. This is due to fuel emanating from the nozzle holes (conical) of the injector or a fuel film in the injector tip that is combusting or pyrolyzing, as reported in Ref. [35]. Decreasing the FIP increases the amount of pool fires at the injector, which persists even in late combustion cycles. The yellow flames that follow the primary combustion leave the combustion chamber filled with hot, burned gases. This is evident in the grey and brown haze in the image, accompanied by small yellow flames. The yellow flames attached to the injector tip likely increased the < 300 nm particles. Berndorfer et al. [36] observed some diffusion combustion in the vicinity of the coked injector tip and reported that the diffusion flame correlates quite well with the PN and soot mass measurements.

Lower FIP could reduce atomization, resulting in thicker, narrower spread fuel films than higher FIP. Therefore, intense, narrow pool fires were observed at 300 bar FIP for advanced SOI timing compared to those at 400 bar FIP. Medina et al. [37] reported that injector tip wetting increased with increasing injected fuel mass, hole length, and lower coolant temperatures. A slightly longer injection duration and a lower spray velocity result in more fuel near the injector tip [38]. Hence, the 300 bar FIP cases showed higher pool fires near the injector tip for retarded SOI timings than the 400 bar FIP cases. PCJ-on cases showed higher pool fires at the injector tip than PCJ-off cases. Lowering the piston temperature reduces the temperature of the air flowing over the injector tip (tumble motion). In-cylinder pressure was slightly (~1 %) lower for PCJ-on than PCJ-off cases at 10° bTDC.

Fig. 10 shows the RF images for PCJ-on and PCJ-off cases. Yellow flames can be distinguished from high-temperature flames in the late combustion cycle by the strong contrast between flame and non-flame regions. Diffusion flames in the bulk mixture occur during the main combustion event and are difficult to distinguish from the high-temperature flame. A small amount of soot particles at high temperatures would give higher illumination intensity. In the late combustion cycle, combustion temperatures are low, and the formed soot cannot oxidize due to reduced oxygen and charge quenching.

At 330 SOI, yellow flames were observed on the piston top in PCJ-on cases. The yellow flames were visible in nearly all combustion images (1 RF). The yellow flames on the piston align with the point where PCJ

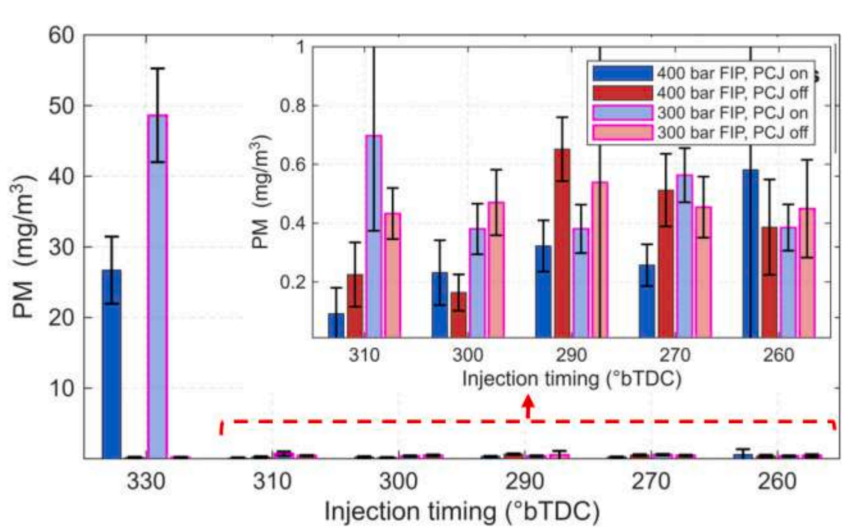

Fig. 8. PM mass at different SOI timings and FIPs in PCJ on/off cases.

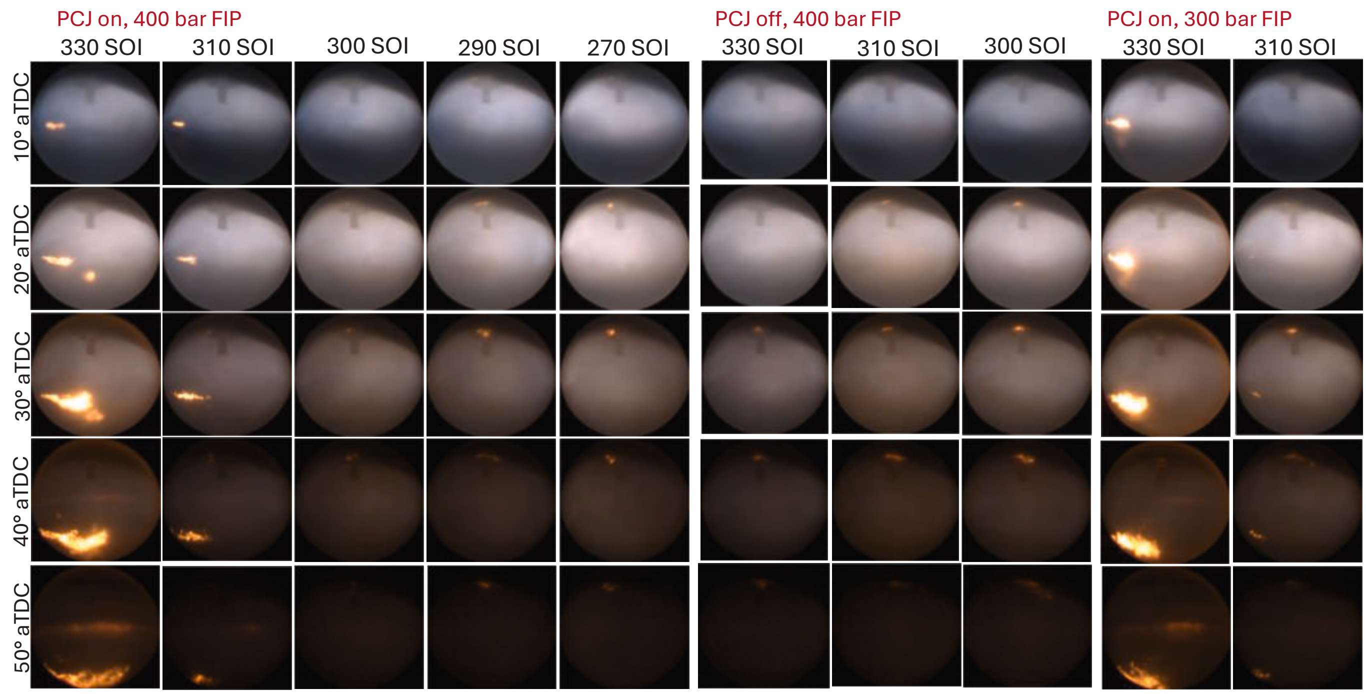

Fig. 9. Random cycle combustion images for PCJ on and off cases at 400 bar FIP.

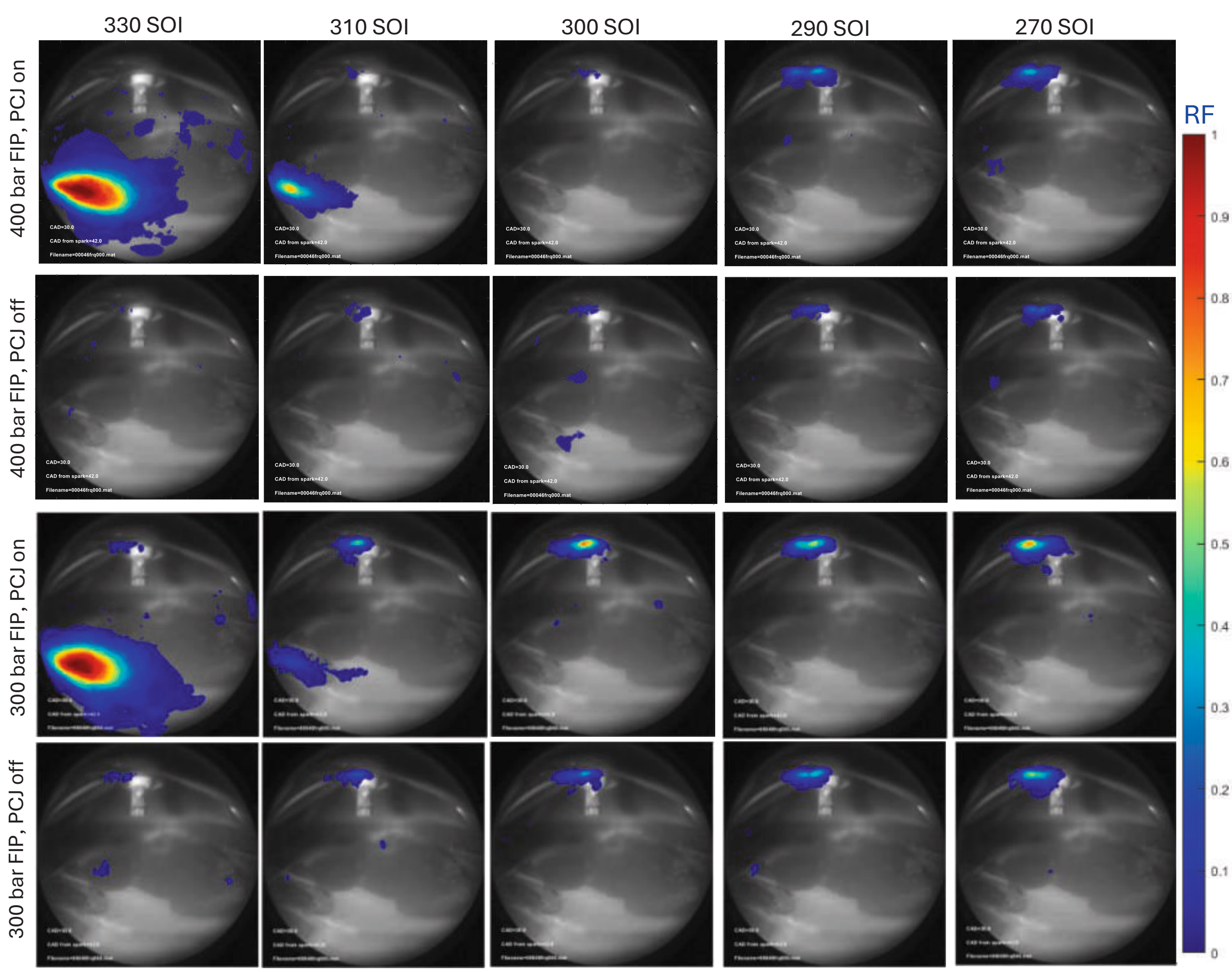

Fig. 10. Relative frequencies of yellow flames at 30°aTDC for PCJ-on and PCJ-off cases from 100 combustion cycles.

contacts the piston at the bottom. This indicates that PCJ generates greater temperature gradients within the piston. Therefore, some fuel films do not evaporate before combustion begins. It appears that one or two spray plumes contribute to pool fires. Yellow flames on the piston persist even during the late combustion cycle (Fig. 11). Abboud et al. [39] observed yellow flames on the piston, which persisted until the exhaust valve opened. Meanwhile, the charge temperature decreases as the piston descends to the bottom dead center, reducing soot oxidation. The 270 SOI indicates that yellow flames frequently occur on the injector tip. Berndorfer et al. [36] reported that residual fuel inside the nozzle holes and rich fuel–air conditions lead to bright diffusion flames. The pool fires were more intense in 300 FIP cases and occurred in every combustion cycle. However, the area of the pool fires on the piston top was lower than that at 400 bar FIP. This indicates that 300 bar FIP results in a narrower fuel film spread on the piston than 400 bar FIP. 300 bar FIP produced more pool fires at the injector tip than 400 bar FIP. Lower FIP increases the amount of fuel around the injector that does not evaporate on time. Comparatively, the RF of yellow flames was lower in the PCJ-off than in the PCJ-on cases, suggesting a thinner fuel film at the injector tip. This correlates well with the PN emissions, which were higher for most PCJ-on cases.

Some random yellow flames were observed in the bulk of the cylinder due to local fuel-rich pockets [40]. The location and intensity of these yellow flames are inconsistent with the combustion cycles. Most of these yellow flames move from the near injector region to the piston, or from the left to the right side of the combustion chamber, as the piston descends. The local fuel-rich pockets depend on air motion, local charge temperature, and other factors [32]. The yellow (diffusion) flames that occur during the main combustion significantly contribute to PN emissions. However, diffusion flames produce much lower PN emissions than pool fires. Improving the fuel–air interaction by charge motion, charge temperature, and injection parameters can reduce the gaseous fuel-rich zones in the bulk. On the other hand, pool fires can be controlled more effectively by optimizing engine parameters than diffusion flames.

Reducing FIP from 400 to 300 bar decreases spray velocity by 13.5 %, while increasing fuel injection duration by 15 %. The spray droplet size could be 7.2 % lower at 400 bar FIP than at 300 bar FIP. The injector tip wetting would be higher due to shorter time between end of fuel injection and start of combustion [14]. Therefore, intensive pool fires were observed at the injector tip for 300-bar FIP but not for 400-bar FIP (Fig. 12). PCJ-off cases showed lower RF than PCJ-on due to reduced tip wetting. RF was very low after 50° crank angles, indicating weak pool fires. Pool fires near the injector tip shift their location due to charge motion in each cycle.

The blue channel (combustion) and the red channel (hot soot) of the natural luminosity are shown in Fig. 13. Red light (750 nm) is 500 times stronger than blue light (450 nm) [41]. The blue flames indicate high-temperature combustion, mainly caused by C_2 and CH radicals, and signify non-sooting combustion [35]. The intensity and spectral content of blackbody radiation depend on the combustion temperature (1100–1700 °C) [41]. The yellow intensity was observed from 8°aTDC to the last frame of the image. It was higher during the main combustion and lower during the late-cycle period. At high temperatures, combustion radicals radiate like a hot blackbody emitter. Hence, very small soot precursors could also produce very high incandescence at red-channel wavelengths. On the other hand, as reported by Singh et al. [35], the side-mounted endoscope did not provide a glimpse of soot during the main combustion event, but soot formed in the late cycle was clearly observed. The measured soot and the occurrence of yellow luminous flames are strongly correlated, as also reported in Ref. [42]. Therefore, it is better to correlate the PN emissions with late-cycle yellow luminosity. 300 SOI showed negligible yellow luminosity in the late cycle (after 25°aTDC). 330 SOI and 270 SOI showed stronger and weaker yellow luminosities, respectively. Therefore, it can be concluded that pool fires on the piston top produce more PN than pool fires on the injector tip.

3.1.4. *Gaseous emissions*

Fig. 14 shows HC and CO emissions at various SOI timings and piston-cooling conditions. HC, PN, and indicated specific fuel consumption (ISFC) exhibited similar trends as SOI varies. The piston temperature decreases by at least 50 K when the PCJ is activated [6], which slows the evaporation of fuel trapped in crevices. Incomplete combustion of fuel within crevices primarily contributes to HC emissions [13]. Wall wetting, local charge stratification, and flame quenching increase CO and HC emissions. Advanced SOI timing directs more fuel to the piston (and into crevices) than retarded SOI timing. When the spray hits the top of the piston, some parcels rebound and strike the liner, while some parcels enter the crevices. When the piston moves up, the fuel parcels on the liner are scraped and brought to the top of the cylinder. During the late combustion cycle, the flame reaches this crevice region and burns the fuel-rich mixture [43]. When the PCJ is off, the piston's temperature is higher. Warmer piston surfaces enhance fuel evaporation and reduce fuel in crevices. Hence, HC emissions were 75 % lower in PCJ-off than in PCJ-on at 330 SOI. Delaying SOI timing could reduce fuel accumulation in crevices because the spray parcels travel farther before striking the piston [13]. Therefore, the effect of piston cooling on HC appears less significant for SOI timing later than 300°bTDC. However, late SOI timing or a longer injection duration causes the spray to strike the liner directly, increasing fuel parcels in the crevices [44]. At optimal SOI timing, PCJ-on cases showed 5–16 % higher HC emissions than PCJ-off cases.

HC emission trends with SOI cases at 300 bar FIP were like those at 400 bar FIP. In most SOI cases under PCJ-on, 300-bar FIP showed higher HC than 400-bar FIP. In contrast, HC was lower under PCJ-off conditions in all SOI cases. It seems that HC and PN did not follow the same trend in PCJ on/off and FIPs. Variations in CO between PCJ-on and PCJ-off cases

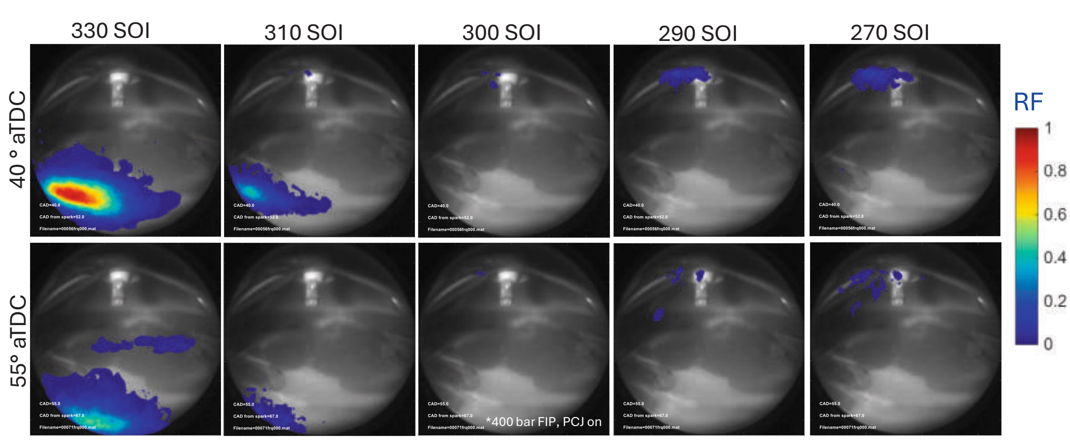

Fig. 11. Relative frequencies of pool fires at late combustion cycles and 400 bar FIP for PCJ-on cases.

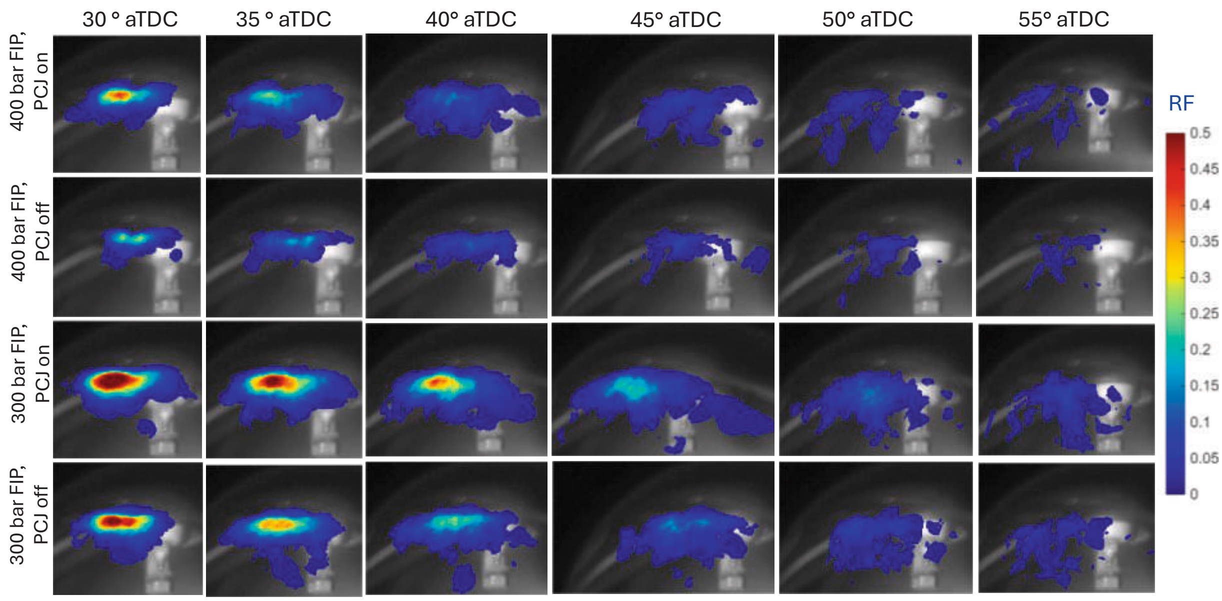

Fig. 12. RF of pool fires near the injector tip for 270 SOI cases (30°aTDC).

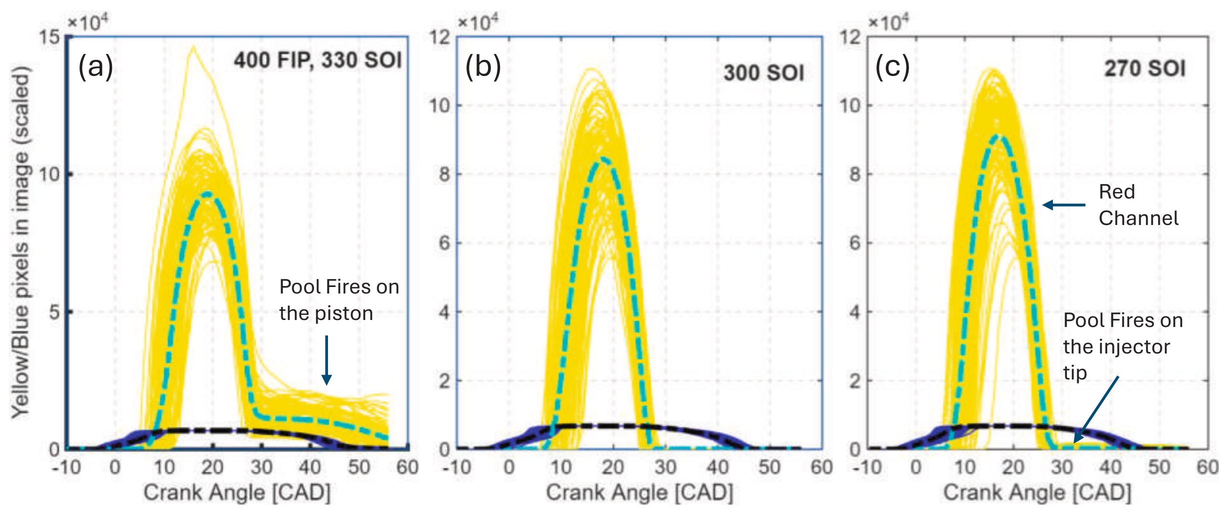

Fig. 13. Red channel of the natural luminosity images for PCJ-on cases from 100 combustion cycles (yellow lines) and average value (green line). Blue lines show non-sooting flames, and the black line represents their average. (Use color version).

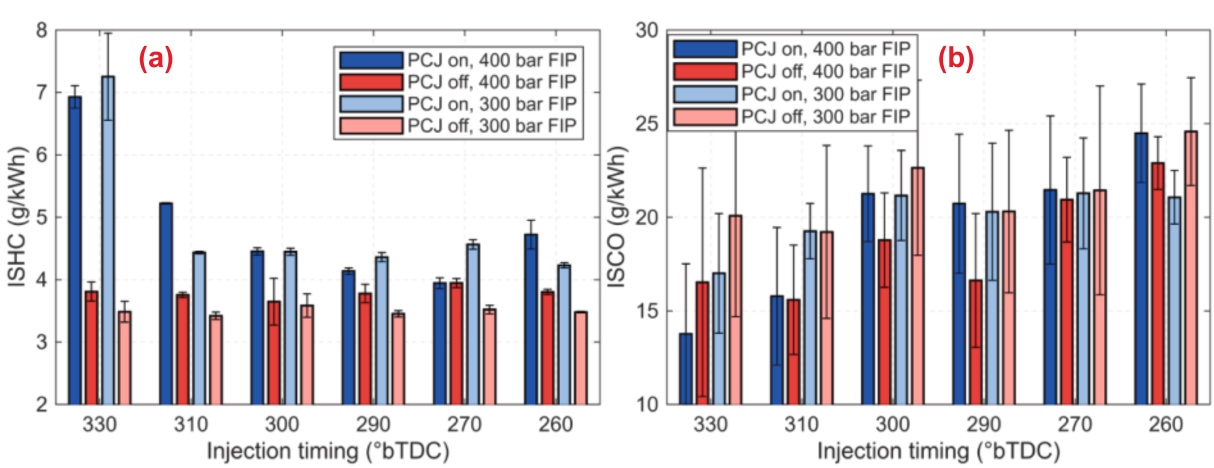

Fig. 14. (a) HC and (b) CO emissions for various SOI timing and FIP at 9 bar IMEP.

were nearly the same (Fig. 14). At delayed SOI timings, CO and NO were higher in the PCJ-off than in the PCJ-on cases (Fig. 15)

Retarded SOI timings resulted in ~ 30 % and ~ 10 % higher CO and NO emissions, respectively, compared to advanced SOI timings. Retarding the injection timing reduces the fuel–air mixing time and alters the interaction with the in-cylinder gas motion, which may lead to fuel-rich regions in the bulk [44]. The CO_2 levels were higher when the PCJ was on than when it was off. CO_2 and PN follow the same trend. More fuel burning and/or improved combustion raise CO_2/kWh levels. The CO/CO_2 ratio was lower at 310 SOI cases and higher at 260 SOI cases. Under pool fire-like conditions, the CO/CO_2 ratio was lower. The CO/CO_2 ratio was lower at 400 bar than at 300 bar FIP cases, indicating improved combustion. Overall, with respect to gaseous emissions, 300 SOI offers the best compromise, yielding moderate levels of NO, CO, and HC.

3.1.5. Fuel consumption, NOx and PN trade-off

330 SOI under PCJ-on conditions showed higher PN and ISFC and lower NO emissions than PCJ-off conditions (Fig. 16). Retarded SOI timings showed higher NO and moderate PN and ISFC values for PCJ on/off cases. Optimal SOI (290°bTDC) timing showed lower PN (1e5 #/cc), NO (9.3 g/kWh), and ISFC (222 g/kWh) than other SOI cases. PCJ-off cases showed lower PN, NOx, and ISFC than PCJ-on cases in advanced SOI cases.

3.1.6. Particle emissions under the endoscope and metal plug conditions

The endoscope was recessed by 2 mm, whereas the metal plug was flash-mounted with the combustion surface. This could slightly alter the charge flow fields and spray dynamics. The endoscope diameter was 12 mm, and the sapphire window thickness was 3 mm. The temperature after the sapphire window was ~ 180 °C, whereas ~ 127 °C for the metal plug case at 12 bar IMEP. This indicates that the temperature of the 12 mm-diameter surfaces could be lower in metal plug cases than in endoscope cases. Hence, there could be slight variations in PN emissions for metal plug and endoscope cases. Only a slight variation in PN was observed when the metal plug was used instead of an endoscope (Fig. 17, a). Sub-10 nm particles showed < 30 % changes, whereas > 23 nm particles showed > 30 % changes between the endoscope and metal plug cases at 9 bar IMEP. Nearly identical PN results were observed for the metal plug and endoscope cases under typical engine load and injection timing conditions (Fig. 17, b).

3.1.7. Particle emissions under medium engine loads with PCJ on

Fig. 18 shows the PN emissions at 12 and 14 bar IMEP conditions. Increasing engine load conditions raise in-cylinder temperatures and fuel evaporation, thereby decreasing PN. However, at 12- and 14-bar IMEPs, advanced SOI timings showed higher PN than optimal SOI timings, like as 9-bar IMEP cases (PCJ-on). Hence, presumably, pool flames exist on the piston top. Therefore, the piston surface temperature is insufficient to eliminate the pool flames on the piston top. SOI timings of 300 and 290°bTDC showed 98.7 % lower PN than the 330 SOI timing. Compared to 9 bar IMEP, SOI timings (300 and 290) showed 53–92 % lower PN at 12 bar IMEP. Higher in-cylinder temperature reduces the formation of local fuel-rich regions and soot. At 14 bar IMEP, SOI timings of 300 and 290°bTDC showed ~ 50 % higher PN than 12 bar IMEP. This could be due to the fuel-rich regions in the cylinder. At 425 bar FIP, SOI timing later than 290°bTDC could result in fuel injection even after 270°bTDC, leading to diffusion flames near the injector tip.

At 12 and 14 bar IMEP, 330 SOI timing PCJ-on cases showed PN emissions 360- and 65-times higher than PCJ-off cases (Figs. 18 and 23). In PCJ-off cases, sub-10 nm particles were 10 times lower, and > 10 nm particles were 100 times lower than in PCJ-on cases. Improved fuel evaporation and fuel–air mixing greatly reduced the soot particles. Hence, PN reduction was ~ 99 % for PCJ-off at 12 and 14 bar IMEP, similar to 9 bar IMEP.

3.2. Campaign 2: High engine loads

The in-cylinder pressure and apparent HRR of the F2 are shown in Fig. 19. The combustion characteristics of the test fuels were nearly identical at typical engine loads. The peak in-cylinder pressure (P_{max}) was ~ 58 bar and ~ 66 bar at IMEPs of 12 bar and 18 bar, respectively. All test fuels showed nearly the same P_{max} across the 14–18 bar IMEP range. The COV_{IMEP} was ~ 0.75 % for the test fuels at 12 bar IMEP and increased to 1.64 % at 18 bar IMEP. Cycle-to-cycle variation in in-cylinder pressure was higher at high engine loads due to stochastic variations in the charge. At high loads, increasing combustion volume (due to later CA_{50}) reduces charge density and flame velocity, increasing the second phase of combustion (CA_{50}–CA_{90}) duration. This could cause more burning of the lubricating oil film [45]. The cylinder liner might be 7 mm more exposed to the flame (considering the CA_{90}) at 18 bar IMEP than at 12 bar IMEP. F2 showed (0.2 CAD) lower ignition lag (ST_CA_{10}) than other test fuels. Lower aromatics promote faster evaporation, and higher *iso*-paraffins burn more quickly for F2 [46].

The variations in in-cylinder pressure and HRR across the test fuels are smaller, as shown in Fig. 20. The CA_{50} was the same for test fuels, resulting in similar HRR characteristics. The peak in-cylinder pressure was 1 bar lower for F1 than for F2 at 12–14 bar IMEP. However, F1 showed slightly higher peak pressure than F2 at 16–18 bar IMEP. P's peak pressures were slightly below the F2 values. Combustion duration (CA_{90}-CA_{10}) was 3 % lower for F2 than for F1 at 12 bar IMEP, and nearly the same at 18 bar IMEP. The CA_{50} was retarded as engine load increased to reduce knock.

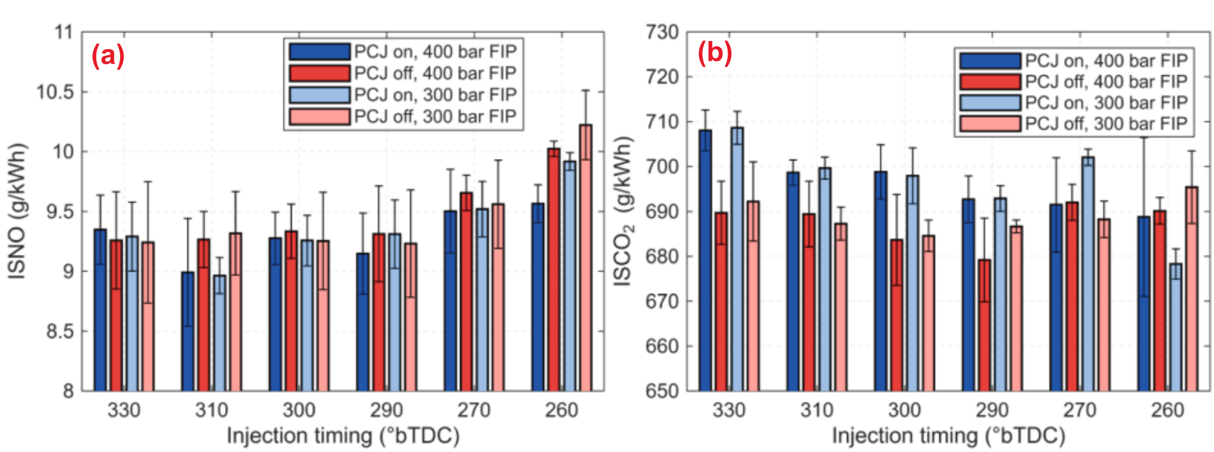

Fig. 15. (a) NO and (b) CO_2 emissions for various SOI timing and FIP at 9 bar IMEP.

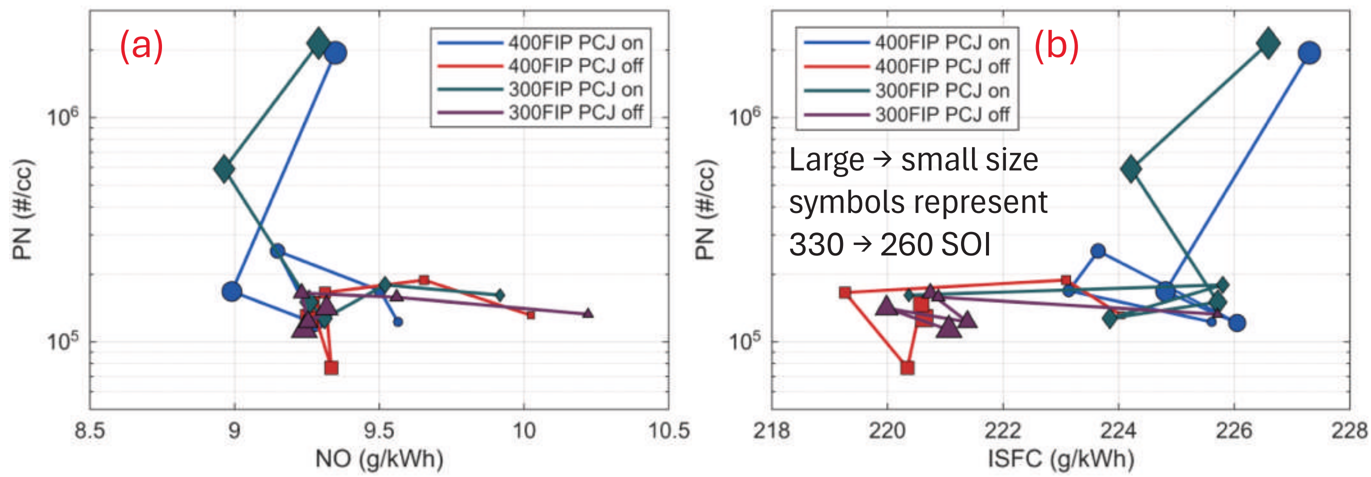

Fig. 16. (a) Relationship between PN and NOx and (b) PN and fuel consumption.

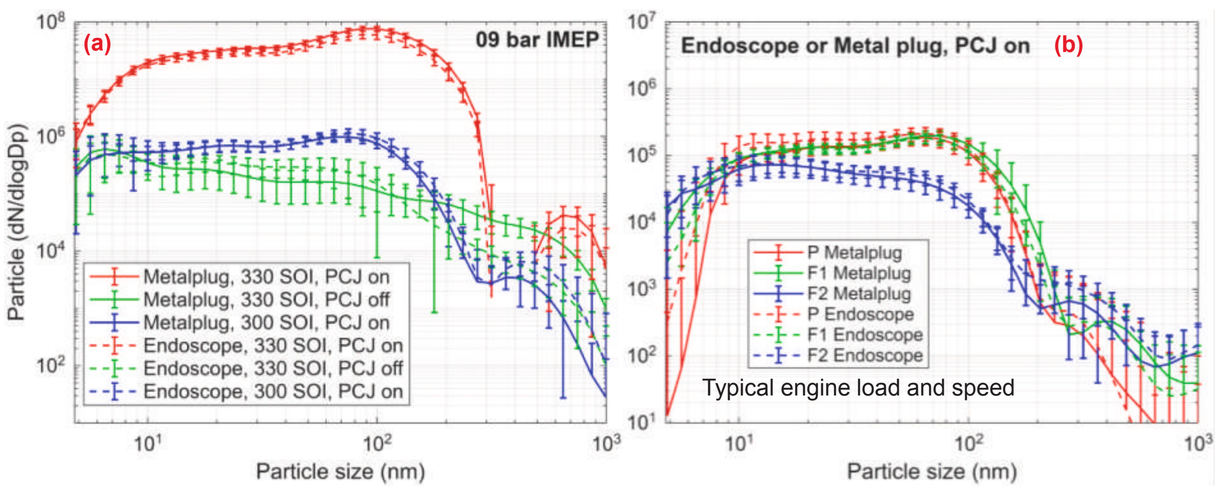

Fig. 17. The influence of the endoscope and the metal plug on particle emissions.

3.2.1. *Energy analysis*

Indicated efficiency for test fuels was nearly the same at typical engine loads (Fig. 21). Exhaust gas and in-cylinder heat transfer losses increase with increasing engine load. These losses account for ~ 60 % of fuel energy. Combustion inefficiency decreases with increasing engine load, as evidenced by reduced HC and CO emissions. Slight variations in combustion inefficiency indicate differences in gaseous emissions among the fuel cases. Less than 4 % of the fuel contributes to gaseous emissions. F2 has a lower T50 and aromatics content than the other test fuels, thereby reducing incomplete combustion. Pumping losses were very low due to boosting.

3.2.2. *Particulate emissions*

Particle and gaseous emissions from the test fuels varied, unlike their combustion characteristics. The variations in emissions reflect changes in combustion quality and chemistry, while stable thermal efficiency indicates that the quantity and timing of energy conversion remained constant. Micro-level factors such as the type of hydrocarbons, local fuel–air mixing, and oxidation process influence the formation of emissions.

Advanced SOI timing and hot-piston conditions could form local, fuel-rich gaseous pockets. These rich pockets undergo pyrolysis, promoting soot precursors. Freshly nucleated nanoparticles are below 10 nm. Fuel's C9+ aromatics could form sub-10 nm particles [14]. F1 and F2 contain more C9+ aromatics. P contains more olefins than F2, increasing pyrolysis at high temperatures. Variation in sub-10 nm particles among the test fuels was 25 % and 15 % at IMEP of 12 and 18 bar, respectively (Fig. 22). It seems that the fuel composition has less influence on sub-10 nm particles at high engine loads. Higher flame temperatures enhance lubricant evaporation on the liner, which partially burns during combustion, thereby increasing soot precursor formation [9]. Retarding CA_{50} generally reduces peak in-cylinder temperature and pressure while increasing exhaust gas temperature due to late heat release. Lower in-cylinder temperatures during the expansion stroke can reduce oxidation of soot formed during combustion, allowing more particles to survive until exhaust valve opening. Hence, the PN at high load is likely influenced by fuel composition, mixture preparation, and reduced in-cylinder soot oxidation. Since all test fuels were evaluated under the same combustion phasing, the reported PN trends represent the combined effects of fuel properties and mixing under realistic operating conditions.

Sub-23-nm particles increased with engine load. Increasing FIP, boost, and combustion temperature results in more sub-23 nm [47]. At 12 bar IMEP, 10–200 nm particles were lower for P than for other test fuels. Furthermore, the concentration of 10–23 nm particles increased with increasing aromatics concentration. Lowering T90 with higher olefins reduces fuel-rich regions [48], decreasing particle formation. At 14 bar IMEP, 10–30 nm particles were lower for P than for other test fuels. The combustion quality of olefins decreases at higher combustion temperatures [48]. Hence, replacing paraffins with olefins and

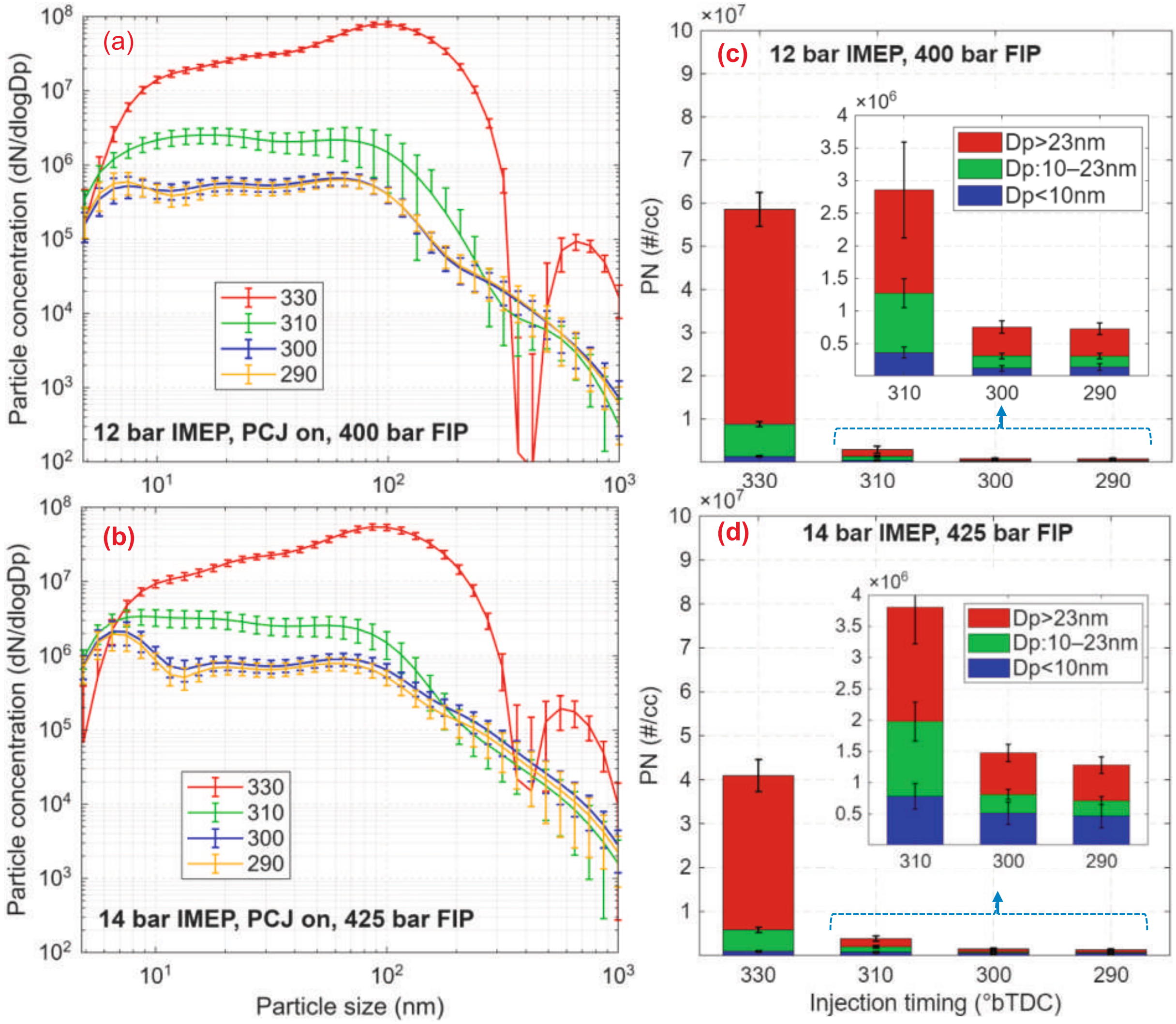

Fig. 18. PN in SOI timing at 12 and 14 bar IMEPs for P under PCJ-on conditions.

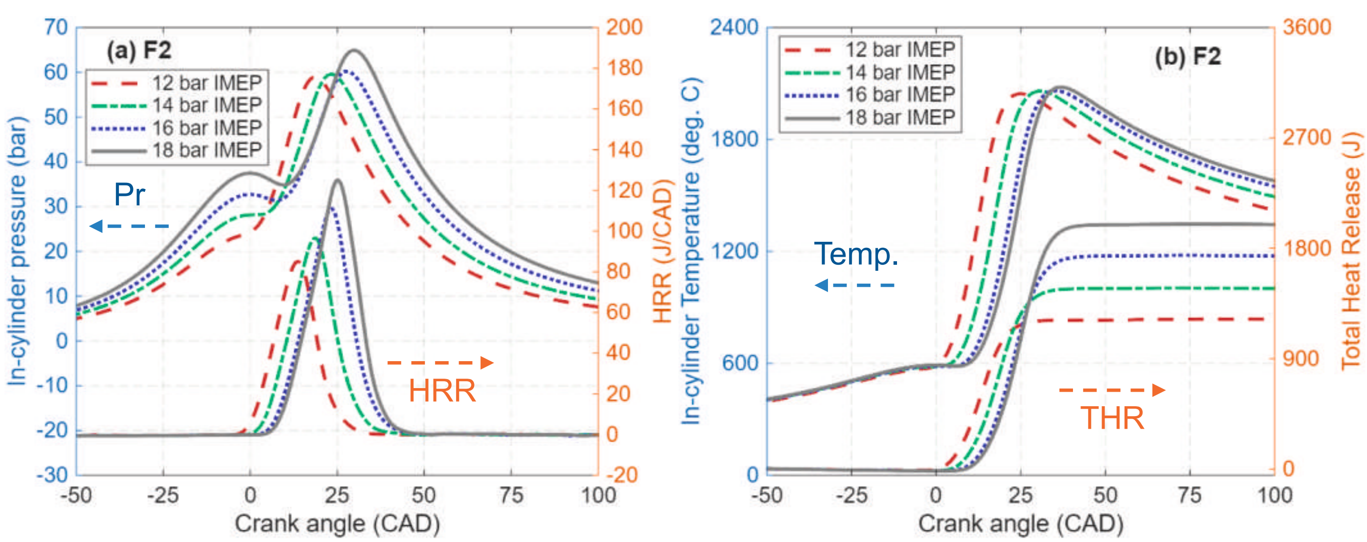

Fig. 19. (a) In-cylinder pressure and HRR for F2, and (b) Mean in-cylinder temperature and total heat release.

naphthene (P) could increase particle formation at high loads. This is shown in Fig. 22(d). Zhang et al. [49] reported that 10–100 nm particles increased with increasing engine load and heavy aromatics in the fuel due to the fuel pyrolysis. F1 showed lower 10–200 nm particles than P at

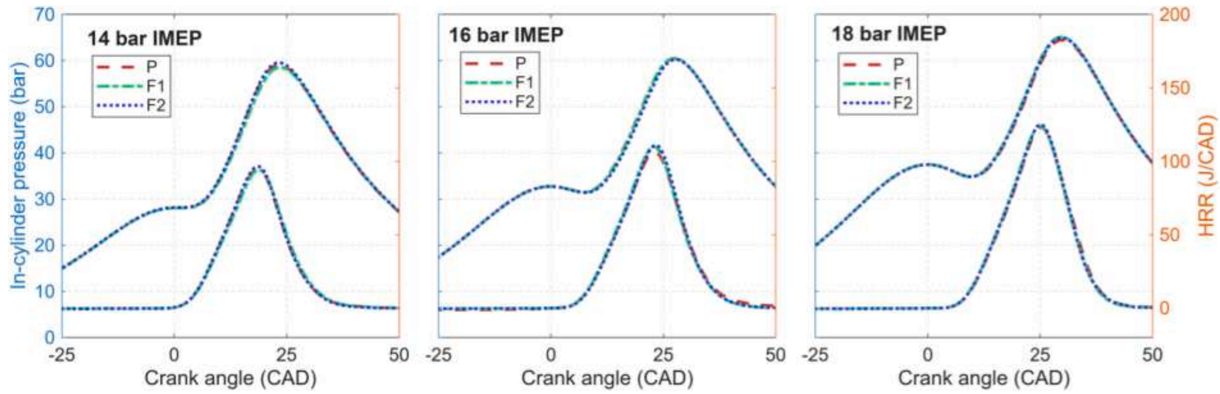

Fig. 20. (a) In-cylinder pressure and HRR for P, F1, and F2 at higher IMEPs.

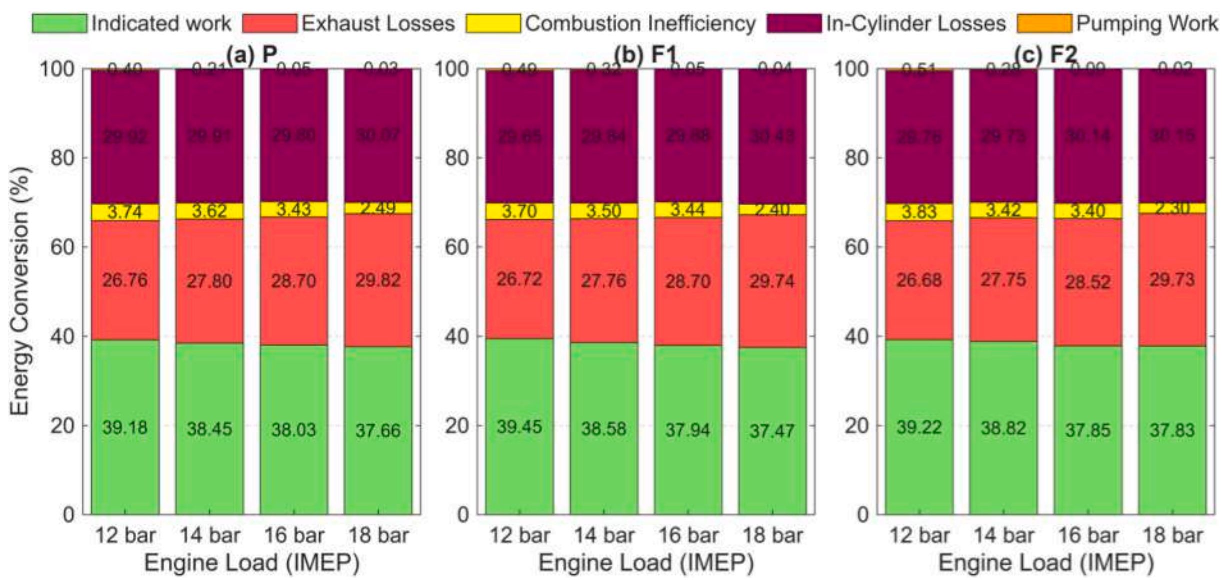

Fig. 21. Energy share analysis for different fuels at high engine loads.

18 bar IMEP, despite having 3 % more aromatics. F1 had a lower T50 and a higher T90 than P. 10–200 nm particles increase with increasing T50, as reported by Qian et al. [46]. Another study [50] reported that increasing olefins and aromatics, along with increasing T90, results in more > 23 nm particles. However, T90 effects on > 23 particles were not observed at 14–18 bar IMEPs. It could be true for < 14 bar IMEP cases [14]. Fuel with lower IBP-T60 temperatures may evaporate quickly due to preferential evaporation, resulting in smaller droplets containing fewer heavier hydrocarbons. Heavier hydrocarbons (T90-FBP), which may indicate the presence of heavy aromatics, could evaporate more efficiently at higher temperatures, resulting in a less fuel-rich mixture. Single-ring aromatics exhibit less pressure dependence in soot formation, whereas olefins show strong pressure dependence [51]. Some cycloalkanes and their reactions that contribute to soot formation depend on combustion temperature [52].

F2 has a higher T90 and FBP than P but contains lower aromatics. Higher T90 and FBP fuel components evaporate more slowly [53]. F2 showed lower > 10 nm particles than P, indicating that fuel evaporation was not a significant issue at 14–18 bar IMEP engine loads (Fig. 23). In this study, the fuel injection ended at ~ 300° bTDC, and the combustion chamber was hot. This condition reduces the fuel film on the piston and injector tip, but local fuel-rich gaseous zones may still exist. The hydrocarbon composition of fuel-rich gaseous zones and their combustion characteristics influence particle formation. F1 showed more 10–100 nm particles than F2 at 14–18 bar IMEP due to aromatics [54]. At high temperatures, olefins break down into reactive radicals and soot precursors [35]. Higher levels of soot precursors accelerate polymerization, increasing PAH levels. Higher naphthene produces more soot at boost conditions [35]. Therefore, olefins, naphthene, and T50 have more influence on 23–200 nm particle formation at 14–18 bar IMEPs.

100–400 nm particles were slightly higher after 12 bar IMEP for the test fuels. The high-pressure high-temperature combustion supports coagulation, increasing aggregate size (~100–500 nm) [55]. 100–400 nm particles were higher for F1 than for F2 at 14 bar IMEP. F1 showed 4–68 % higher aggregates (200–1000 nm) than P at 12 and 14 bar IMEPs. F2 exhibited 6–35 % higher aggregates than the other fuels at 16 and 18 bar IMEPs. It seems that for F1 and F2, soot particles collide rapidly and stick together, forming larger aggregates than for P. Particles in the 150–400 nm range were higher for F2 than for the other fuels, and this was linearly correlated with FBP and C10 + aromatics.

Particles > 10 nm were 25–40 % of total PN at 12 bar IMEP, whereas only 11–20 % at 18 bar IMEP. Particles < 10 nm increased faster than those > 10 nm as engine load increased. High combustion temperatures can burn the lubricating oil film, increasing sub-10 nm particles, as reported in Ref. [10]. Apicella et al. [45] reported that incomplete combustion of oil leads to soot formation only at higher temperatures.

Gasoline particulate filters (GPFs) are highly effective at trapping particles and typically achieve ~ 99 % filtration efficiency for most solid particles; their efficiency for sub-10 nm particles can be lower (~50 %), depending on the filter loading state [56]. Catalytic converters can

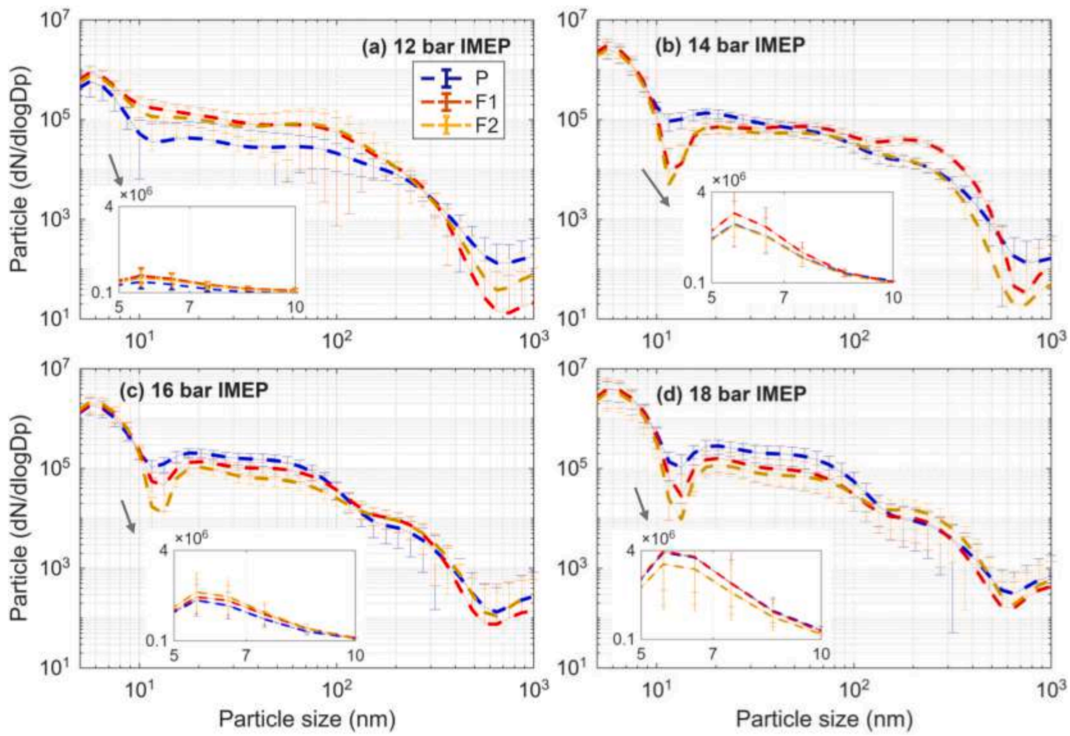

Fig. 22. PN for all three test fuels at 12 and 18 bar IMEP.

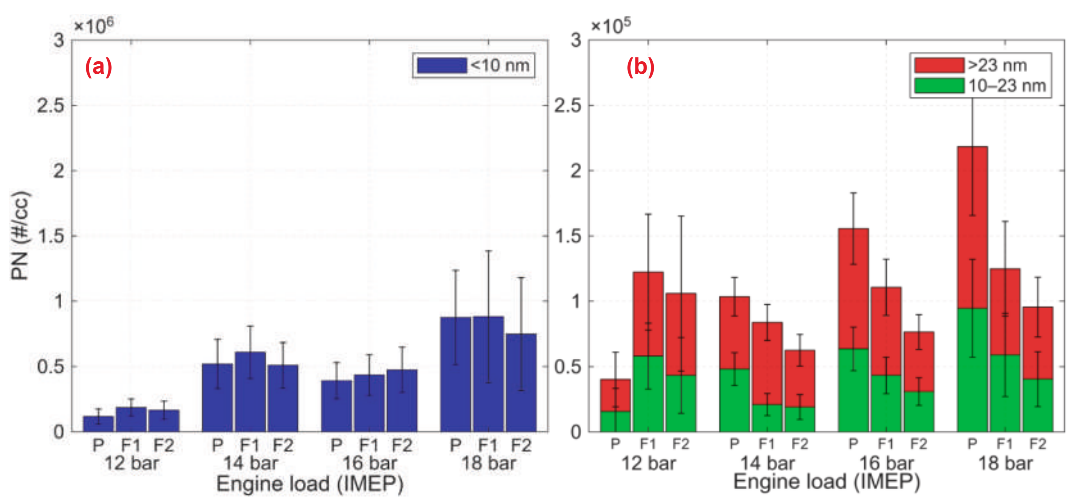

Fig. 23. Sub-10 nm, 10–23 nm, and > 23 nm particles for different fuels and engine loads.

reduce sub-10 nm particles by ~ 80 % [57]. However, reducing > 10 nm particles in the engine remains important because it reduces reliance on the aftertreatment system. Particles 10–23 nm increased by 3.5–6.5 times as engine load increased. Particles > 23 nm increased 4-fold for P but did not change for F2. Therefore, PN measurements from 10 nm onward will increase the total PN under the Euro 7 standard because particles larger than 10 nm are considered for the PN (6×10^{11} #/km). Vans require about 0.4 kWh of indicated engine energy (power) to travel 1 km. At 14 bar IMEP, P showed 2.75×10^{11} particles per kWh, which is 20 % higher than F2. Similarly, at 18 bar IMEP, P and F2 showed 4.7×10^{11} and 2.74×10^{11} particles per kWh, respectively.

PM increased by 89–140 % when increasing the engine load from 12 to 18 bar IMEPs (Fig. 24, a). At 14 bar IMEP, P and F1 showed higher PM due to more 200–1000 nm particles. Even fewer large particles would significantly increase PM. Slightly advancing the CA_{50} might help burn the particles for P and F1 cases. However, gravimetric PM measurements would provide a more realistic analysis. In contrast, F1, with high aromatics and low olefin content, exhibited lower PM (due to lower 200–1000 nm particles) at 18 bar IMEP.

Variations in PM with respect to sampling time increased as engine load increased (Fig. 24, b). PM versus time trends were similar for test fuels at typical loads. Fuel that hits the liner may accumulate in the crevice region if it is not evaporated. Eventually, it will react/ not react with an oil film, forming a fuel–oil mixture and deposits [58]. Fuel evaporation and adhesive/ cohesive characteristics determine the fuel–oil mixture or deposits. Wall wetting and fuel-lubricant interaction might increase with increasing fuel mass. Heavy aromatics and sulfur could form deposits [58]. Fuel-oil mixtures often burn, which increases PM spikes. They form deposits if not burned often, and detached deposits lead to pre-ignition. Pre-ignition was not observed in this study.

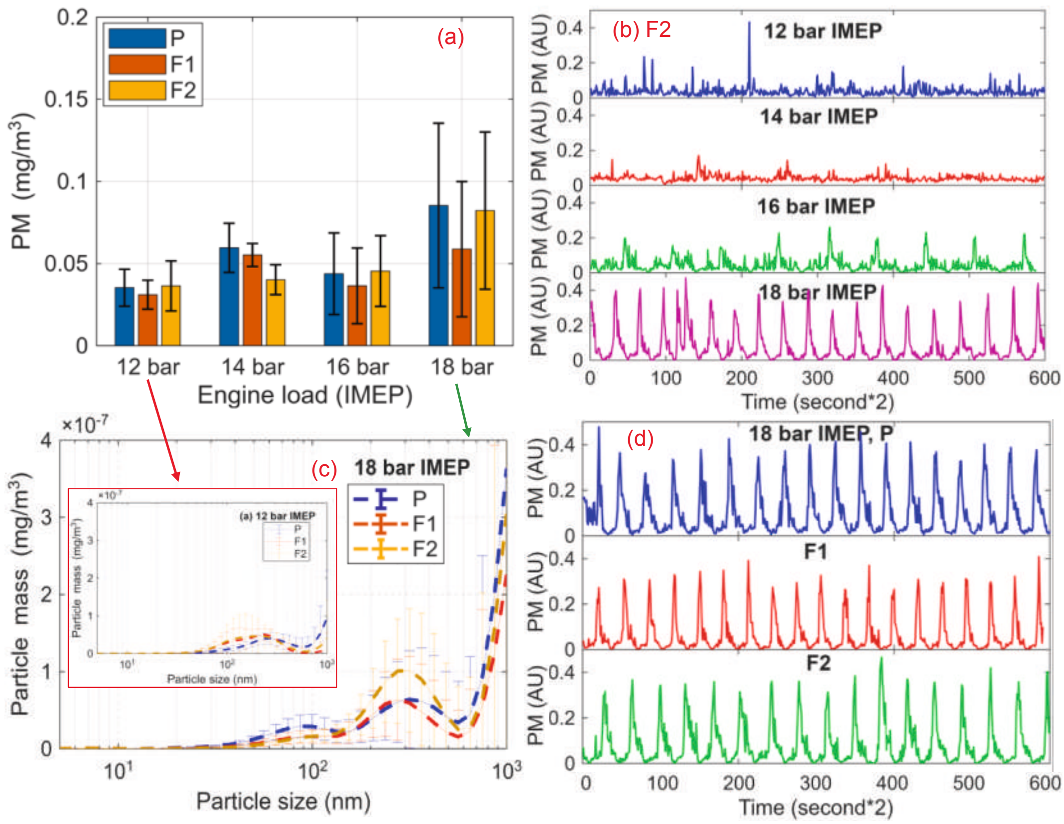

Fig. 24. (a) PM for different engine loads for test fuels, (b) PM mass vs. time for F2, (c) particle mass concentration at 18 bar IMEP, and (d) PM vs. time for test fuels at 18 bar IMEP.

Periodic shedding or detachment of soot deposits from wall surfaces and the injector tip can cause PM spikes.

The PN and PM against sampling time trends differ. Since the particles are assumed to be of the same density, PM is mainly contributed by larger particles. It seems that the contribution of sub-23 nm particles to PM mass was lower than that of > 23 nm particles. At 12 bar IMEP, a few spikes were observed in PM. Less intense PM spikes were observed at 14- and 16-bar IMEPs. At 16 bar IMEP, PM spikes occurred often, but their intensities were lower than at 18 bar IMEP. 18-bar IMEP showed PM spikes for all test fuels. PM spikes rise rapidly, then decrease slowly. At 18 bar IMEP, >23 nm particles account for 7–12 % of total PN. > 23 nm particles are typically associated with soot and agglomerates.

Variations in fuel injection mass, mixing, and local fuel-rich regions lead to more particles in some cycles. Partial oxidation of oil-fuel mixtures shows ripples in the in-cylinder pressure curve and increases PN. Under knocking and pre-ignition conditions, rapid heat release and elevated local temperatures can alter soot formation and oxidation, potentially increasing PM. Ripples in the pressure curve and peak cylinder pressure for F2 at 18 bar IMEP are shown in Fig. 25. Since PM spikes occur every ~ 17 s, there could be a knock in every ~ 280 combustion cycles. Fig. 25 shows one or two knock cycles in 250 combustion cycles. Engine knock increases > 23 nm particles, as shown in Fig. A1 (in the Appendix).

3.2.3. *Performance and gaseous emissions*

Indicated thermal efficiency was ~ 2 % higher at 12 bar than at 18 bar IMEP for all test fuels. Variations in ISFC for the test fuels were minimal at typical loads. P showed 0.8 % higher ISFC than the other test fuels only at 12–14 bar IMEP. F1 showed a 2 % increase in ISFC when IMEP rose from 12 to 18 bar. While the increase in ISFC was ~ 1 % for P and F2. Retarded CA_{50} reduces effective brake power and increases heat transfer losses (2 %) and exhaust gas heat losses (3 %). HC decreased by ~ 1.5 times for test fuels during IMEP rise (Fig. 26). Increasing air temperature and FIP enhance fuel evaporation and air–fuel mixing, reducing HC emissions. Additionally, retarded combustion facilitates the oxidation of HC species originating from crevice regions during the late combustion cycle. F2 exhibited 2–10 % lower HC than P. Decreasing T50-T90 of fuel resulted in lower CO and HC emissions for F2 [48]. P's higher olefins could potentially increase HC compared to F1 [53], but in some cases, F1 showed higher HC due to the higher aromatics and T90.

Local fuel-rich zones, oxygen deficiency, and combustion temperature influence CO formation [59]. CO increased and NO decreased with increasing engine load (Fig. 27), indicating fuel-rich regions. CO emissions form when fuel-rich regions exist in the cylinder. This region lacks oxygen, so the fuel does not fully burn to CO_2, indicating incomplete combustion. 16 bar IMEP showed 5–11 % higher CO than 12 bar IMEP cases. A 20–36 % reduction in CO emissions was observed at 18 bar compared to 16 bar IMEP. If the temperature drops too quickly, CO can freeze and not oxidize to CO_2. Retarded combustion keeps the gas hotter for longer, aiding CO oxidation. Decreasing HC and CO and increasing NO indicate a reduction in fuel-rich zones at 18 bar IMEP. F1 and F2 showed 5–9 % lower CO emissions than P, owing to lower levels of unsaturated hydrocarbons. Lower T40 to T60 (F2) enhances air–fuel mixing, resulting in lower CO and HC emissions [46]. Lowering aromatics with higher T90 reduces CO emissions [53]. Hence, F2 showed lower CO than P.

Retarded CA_{50} helps control the peak in-cylinder temperature and its residence time, reducing knock and NO formation [60]. A reduction in NO was observed from 12 to 18 bar IMEP. Reducing local fuel-rich regions helps to reduce the CO emissions at 18 bar IMEP. Hence, improved fuel–air mixing and retarded combustion phasing reduce NO and CO emissions.

P showed 4.3 % higher NO than F2 at 12 bar IMEP. Olefins and naphthene can increase peak temperatures due to their higher reactivity

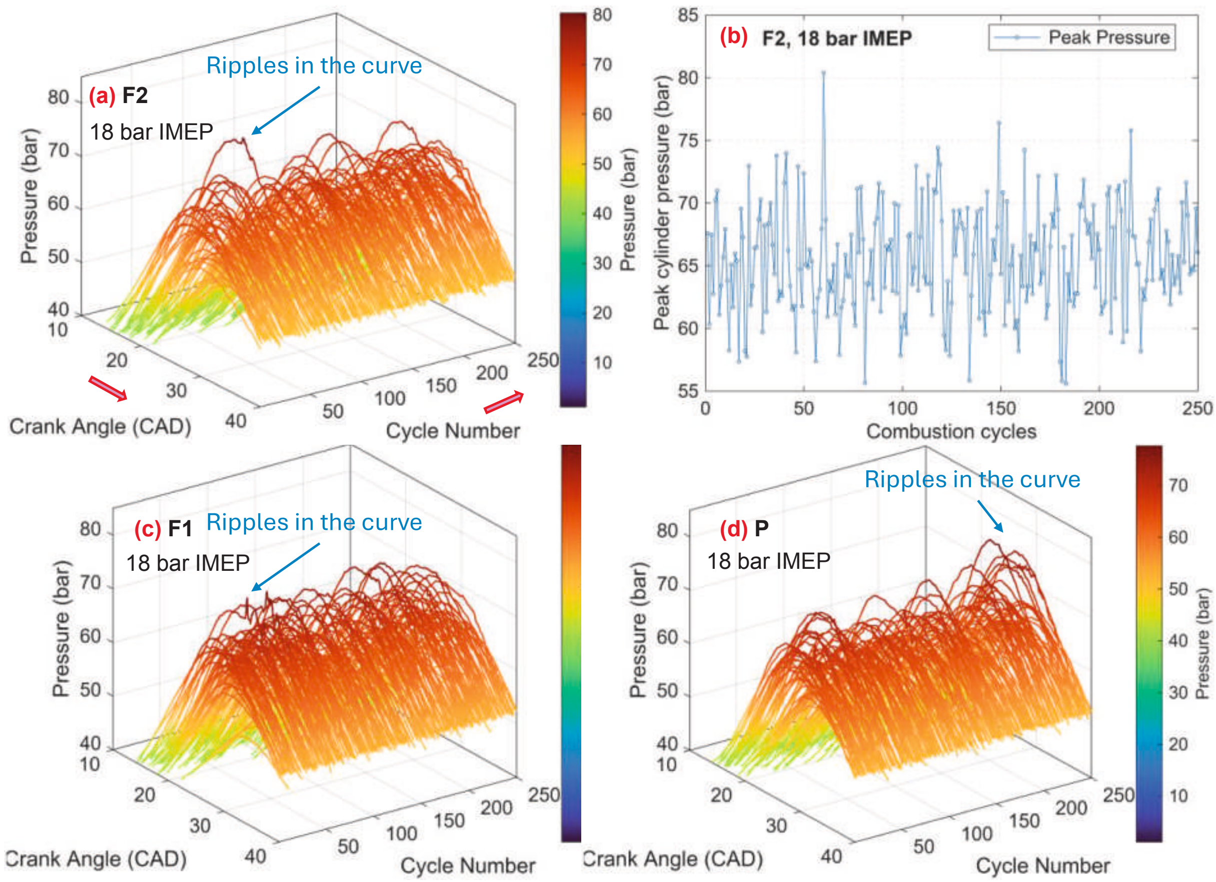

Fig. 25. Ripples in the pressure curve at 18 bar IMEP for test fuels.

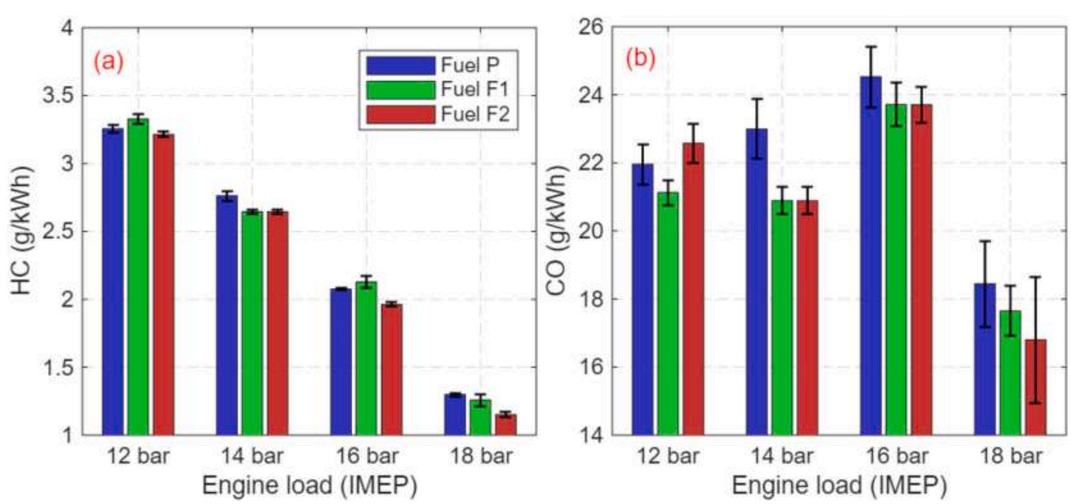

Fig. 26. (a) THC and (b) CO for different engine loads.

and faster combustion rates than paraffins. Increasing olefins increases NO due to their greater reactivity, whereas aromatics have no significant effect [53]. Therefore, P could experience greater pyrolysis at high engine loads than other test fuels. CO and CO_2 concentrations in the exhaust gas exhibited opposite trends with respect to IMEP. CO_2 concentration decreased from 12 to 16 bar IMEP and then rose. Decreasing aromatics and olefins in gasoline (F2) slightly reduces CO_2 [48]. Increasing CO oxidation to CO_2 reduced the O_2 concentration at 18 bar IMEP. The CO/CO_2 ratio and O_2 were ~ 25 % and ~ 15 % lower at 18 bar IMEP compared to 14–16 bar IMEP. ~ 16 % higher exhaust O_2 concentration was observed at 14–16 bar IMEP than at other engine loads. Slightly advancing the CA_{50} at 14 and 16 bar IMEP could improve CO oxidation by raising the combustion temperature. CO/CO_2 ratio was ~ 4 % lower for F1 and F2 than for P at 14–18 bar IMEP. Notably, HC and CO_2 emissions trends follow the PN emissions trend. However, they did not show the same intensity as PN with respect to SOI timings.

3.2.4. *Fuel consumption, NO, and PN trade-off*

All particle sizes and particles > 10 nm, relative to NO and ISFC, are shown in Fig. 28. Decreases in NO and increases in PN were observed as

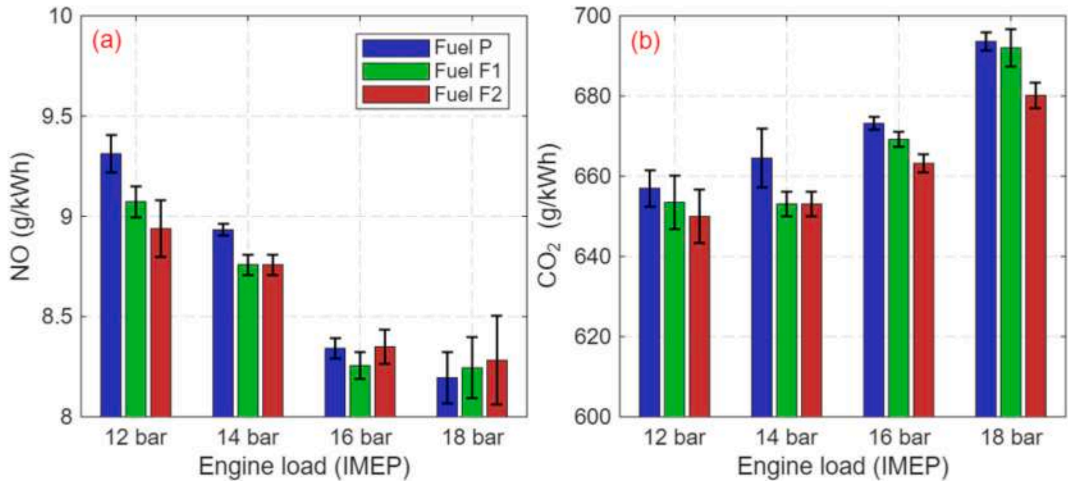

Fig. 27. (a) NO and (b) CO_2 for different engine loads.

IMEP increased. F2 showed lower NO and PN levels than the other test fuels. F2 has a lower T60, thereby improving fuel–air mixing. The improved premixed combustion can reduce the high-temperature residence time. The combustion duration was 3 % lower for F2 than F1 at 12 bar IMEP, whereas the same at 18 bar IMEP. Lower FBP and C9+ aromatics (P) reduce PN at 12 bar IMEP. ISFC and total PN were lower at 12 bar IMEP and increased as IMEP increased. Higher C9+ aromatics increase > 10 nm particles even though the ISFC was lower at 12–14 bar IMEPs. Fuel (F2) with lower vapor pressure reduces PN [14].

4. Limitations of the study

The PCJ reduces piston temperature but slightly lowers liner and injector tip temperatures due to the tumble-charge motion. Hence, this study accounts for all these effects on PN emissions, not just piston temperature. At high loads, PCJ is essential for piston durability. This study demonstrates that PCJ affects engine-out PN emissions and does not recommend disabling the PCJ at high loads. Turning the PCJ on or off based on online piston temperature is challenging. Using optimal SOI when the PCJ is on can reduce PN emissions.

DMS500 could not distinguish between volatile and solid particles in the exhaust gas. Sub-23 nm particles are mostly volatile and originate from oil and fuel sources. However, significant solid particles may also be present in that range. The contribution of lubricating oil to sub-10 nm particle formation is plausible but was not directly quantified in this study. Lubricating oil consumption and elemental analysis of oil-derived particles, which would indicate actual oil film burning/evaporation, were not performed. The pyrolysis of the lubricating oil film and the formation of sub-10 nm particles have not been established in this work. At high loads, the sources of sub-23 nm particles are more quantified.

5. Conclusions

The effects of piston cooling on PN emissions were analyzed at medium engine loads in a single-cylinder GDI engine. SOI timing significantly affects PN emissions compared to FIP.

- The advanced SOI timing showed ~ 50 times higher PN compared to optimal SOI timing in PCJ-on cases. Without PCJ, the advanced SOI timing showed ~ 10 times lower PN than the optimal SOI timing. At 300 SOI timing, FC and PN emissions were slightly higher for PCJ-on than PCJ-off cases.
- Pool fires on the piston and higher PN emissions were observed in PCJ-on cases. Pool fires on the injector tip were observed in both PCJ-on and PCJ-off cases, and they became more prominent with retarded SOI timing. Increasing the air temperature flowing near the injector tip could reduce the pool fires.

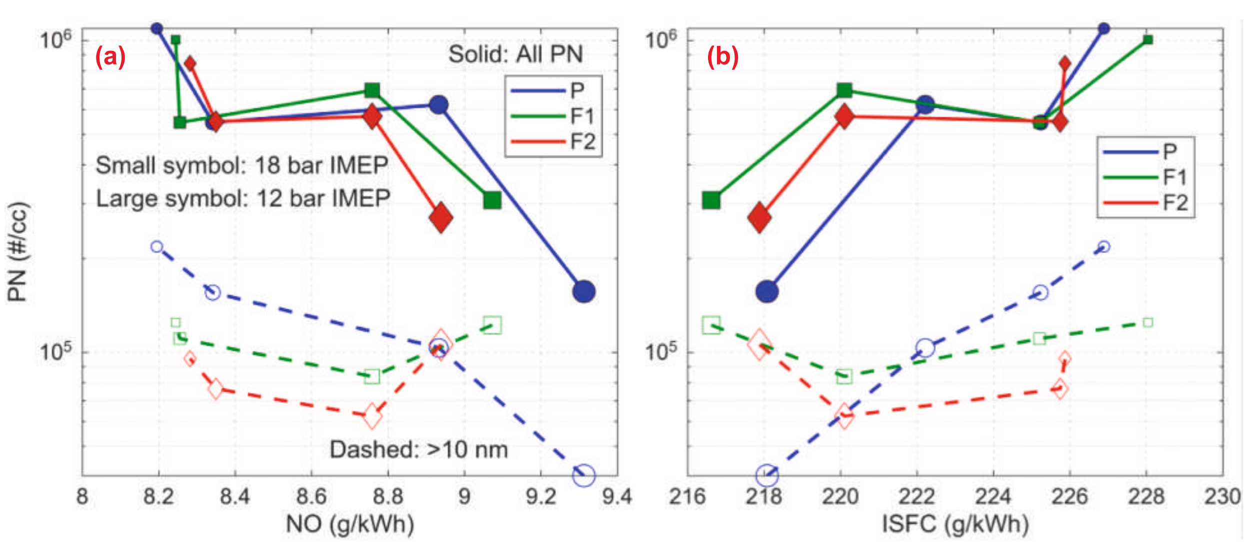

Fig. 28. PN-NO trade-off and PN vs. ISFC relationship.

- The diffusion flames within the bulk of the cylinder were lower, but their contribution to PN remained significant. Combustion with visible diffusion flames resulted in ~ 50 % higher PN than in cases without yellow flames. Combustion with pool fires exhibited about ~ 30 times higher PN compared to combustion with diffusion flames.

The effect of gasoline formulation on particulate emissions was studied at high engine loads. Fuel P was rich in olefins and naphthene, F1 had more aromatics, and F2 had more paraffins compared to each other.

- Three test fuels exhibited nearly identical combustion characteristics and indicated thermal efficiency of 37–39 %. Fuel properties significantly affect CO and PN emissions. P exhibited higher HC and CO emissions than other test fuels.
- Replacing 6.3 % olefins and 3.5 % naphthene (P) with 8 % paraffins and 2.5 % aromatics (F1) decreased 10–100 nm particles with increasing engine load. F1 contained higher aromatics, yielding higher PN at 12 bar IMEP than P. The aromatics' influence on 80–400 nm particle formation appears to decrease with increasing engine load. Since the fuel injection ends at 300° bTDC, air–fuel mixing could be good.
- Replacing 4.5 % aromatics and 2 % naphthene (F1) with olefins and paraffins (F2) showed slightly lower 10–100 nm and higher 100–1000 nm particles. Increasing paraffins and olefins while reducing aromatics helps lower PN emissions at 14–18 IMEPs under no-pool-fire-like conditions.
- Replacing 2 % aromatics, 2.3 % olefins, and 5.1 % naphthene (P) with paraffins (F2) helps reduce > 10 nm particles by 38–56 % at 14–18 bar IMEP. Aromatics' contribution to PN emissions remained consistent, while olefins' and naphthene's contributions increased with increasing engine loads.

CRediT authorship contribution statement

M. Krishnamoorthi: Conceptualization, Data curation, Formal analysis, Investigation, Methodology, Software, Validation, Visualization, Writing – original draft. **Petter Dahlander:** Writing – review & editing, Supervision, Resources, Project administration, Methodology, Conceptualization. **Ayolt Helmantel:** Writing – review & editing, Validation, Resources, Methodology, Conceptualization. **Nika Alemahdi:** Resources, Methodology. **Kalle Lehto:** Writing – review & editing, Validation, Resources.

Declaration of competing interest

The authors declare that they have no known competing financial interests or personal relationships that could have appeared to influence the work reported in this paper.

Acknowledgements

Aurobay, Neste, Chalmers, FFI and the Swedish Energy Agency support this work (P2021-00377). The authors gratefully acknowledge the assistance of Mats Andersson, Anders Mattsson, Timothy Benham, and Robert Buadu in this work.

Appendix

PN spikes under engine knock conditions are shown in Fig. A1. The pressure data show combustion, knock, and motoring conditions. PN with respect to time changed only a little during normal combustion. Knocking causes PN spikes, which could be due to higher temperature and vibration. The vibration could detach soot from the injector and liner surfaces. Piston ring vibration can cause more oil to enter the combustion chamber, resulting in PN emissions.

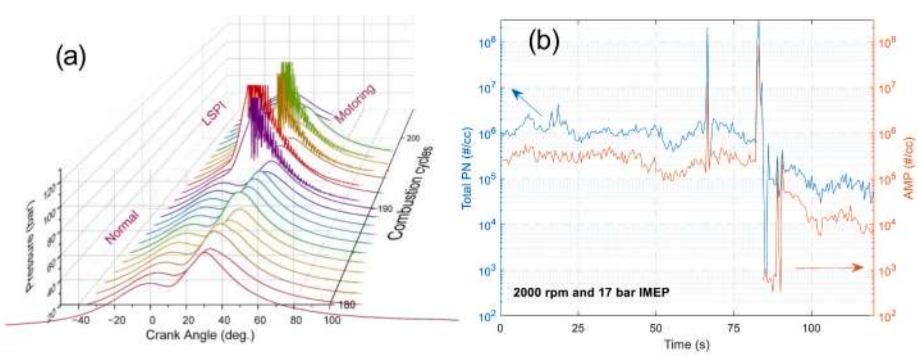

Fig. A1. Pressure during the low-speed pre-ignition under Miller cycles (a). The peak pressure is saturated at ~ 115 bar due to the charge amplifier setting. Total PN and > 23-nm particles (AMP) under normal, LSPI, and motoring conditions (b). LSPI somehow affects PN. AMP line discontinues at the onset of motoring.

Cycle-to-cycle variations in combustion cycle images are shown in Fig. A2. The area and intensity of the yellow flames vary slightly from cycle to cycle.

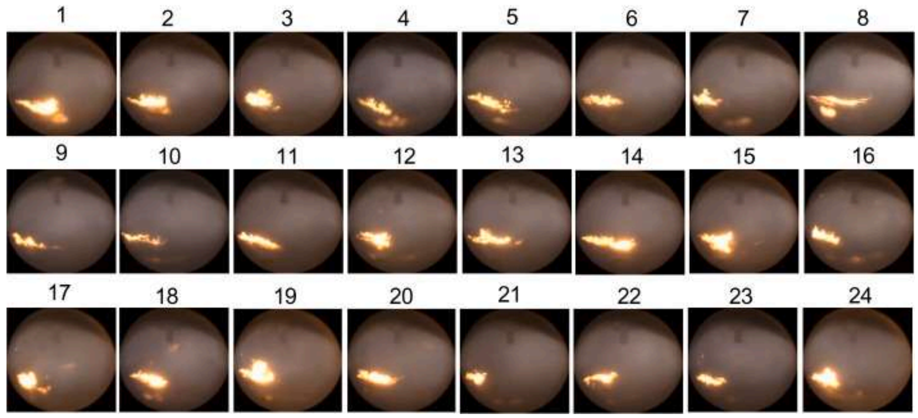

Fig. A2. Combustion images ataTDC for 400 bar FIP and 330 SOI. Combustion images from cycle 1 to cycle 24.

Data availability

Data will be made available on request.

References

[1] Javanshayani F, Shamekhi AH. Modern gasoline direct-injection engines: Key challenges and mitigation pathways: a critical review. Int J Engine Res 2026;27:992–1020. https://doi.org/10.1177/14680874251382740.

[2] Albrecht M, Deeg H-P, Schwarzenthal D, Eilts P. Investigations of the emissions of fuels with different compositions and renewable fuel components in a GDI engine. SAE Technical Paper 2020. https://doi.org/10.4271/2020-01-0285.

[3] da Silva G, Bozzelli JW. On the reactivity of methylbenzenes. Combust Flame 2010;157:2175–83. https://doi.org/10.1016/j.combustflame.2010.06.001.

[4] Hopf A, Kraemer F, Turner cEng P, Weber C. CFD simulation of oil jet piston cooling applied to pistons with cooling gallery. SAE International Journal of Advances and Current Practices in Mobility 2022;5:2022-01–0210. Doi:10.4271/2022-01-0210.

[5] Vinaya murthy V, Sithick basha A, Dharan R B, Rengaraj C, Vignesh AC. Investigation of solenoid-controlled piston cooling jet benefits for a 1.5l, 3 cylinder Tcic diesel engine. SAE Technical Paper, 2023. Doi:10.4271/2023-01-0230.

[6] Luff DC, Law T, Shayler PJ, Pegg I. The effect of piston cooling jets on diesel engine piston temperatures, emissions and fuel consumption. SAE Int J Engines 2012;5:1212. https://doi.org/10.4271/2012-01-1212.

[7] Najafabadi MI, Mirsalim M, Hosseini V, Alaviyoun S. Experimental and numerical study of piston thermal management using piston cooling jet. J Mech Sci Technol 2014;28:1079–87. https://doi.org/10.1007/s12206-013-1183-7.

[8] Kelleher J, Ajotikar N. Piston cooling nozzle oil jet evaluation using CFD and a high speed camera. SAE Int J Commer Veh 2016;09:8100. https://doi.org/10.4271/2016-01-8100.

[9] Apicella B, Catapano F, Di Iorio S, Magno A, Russo C, Sementa P, et al. Impact of fuel and lubricant oil on particulate emissions in direct injection spark ignition engines: a comparative study of methane and hydrogen. Fuel Process Technol 2024;265:108144. https://doi.org/10.1016/j.fuproc.2024.108144.

[10] Yi H, Seo J, Yu YS, Lim Y, Lee S, Lee J, et al. Effects of lubricant-fuel mixing on particle emissions in a single cylinder direct injection spark ignition engine. Scientific Report 2022;12:18. https://doi.org/10.1038/s41598-021-03873-w.

[11] Zhang M, Hong W, Xie F, Su Y, Han L, Wu B. Experimental investigation of impacts of injection timing and pressure on combustion and particulate matter emission in a spray-guided GDI engine. Int J Automot Technol 2018;19:393–404. https://doi.org/10.1007/s12239-018-0038-8.

[12] Jose J, Parsi A, Shridhara S, Mittal M, Ramesh A. Effect of fuel injection timing on the mixture preparation in a small gasoline direct-injection engine. SAE Technical Paper 2018. https://doi.org/10.4271/2018-32-0014.

[13] Muniappan K, Dahlander P, Helmantel A, Alemahdi N, Lehto K. Effect of renewable fuel blends on particulate emissions in warm-up conditions in a GDI engine. SAE Technical Paper 2026. https://doi.org/10.4271/2026-01-0304.

[14] Muniappan K, Dahlander P, Helmantel A, Alemahdi N, Lehto K. Effect of renewable fuel blends on particulate emissions under medium engine load and injector coking conditions in a GDI engine. SAE Technical Paper 2026. https://doi.org/10.4271/2026-01-0301.

[15] Qiu S, Wang S, Nour M, Li X, Xu M, Wang L, et al. Experimental study on flow fields of spray impingement under flash boiling conditions. Energy 2025;318:134748. https://doi.org/10.1016/j.energy.2025.134748.

[16] Nour M, Cui M, Zhang W, Fu J, Luo X, Qiu S, et al. Enhancement of ABE fuel combustion and emissions in simulated cold-start GDI conditions: the impact of flash boiling injection. Energy 2025;328:136585. https://doi.org/10.1016/j.energy.2025.136585.

[17] Abdellatief TMM, Ershov MA, Makhmudova AE, Kapustin VM, Makhova UA, Klimov NA, et al. Novel variants conceptional technology to produce eco-friendly sustainable high octane-gasoline biofuel based on renewable gasoline component. Fuel 2024;366:131400. https://doi.org/10.1016/j.fuel.2024.131400.

[18] Lee Z, Park S. Effects of fuel composition and engine operating conditions on particle number index in a direct injection spark ignition engine. Energ Conver Manage 2021;243:114428. https://doi.org/10.1016/j.enconman.2021.114428.

[19] Puricelli S, Casadei S, Bellin T, Cernuschi S, Faedo D, Lonati G, et al. The effects of innovative blends of petrol with renewable fuels on the exhaust emissions of a GDI Euro 6d-TEMP car. Fuel 2021;294:120483. https://doi.org/10.1016/j.fuel.2021.120483.

[20] Etikyala S, Koopmans L, Dahlander P. Effect of renewable fuel blends on PN and SPN emissions in a GDI engine. SAE Technical Paper 2020. https://doi.org/10.4271/2020-01-2199.

[21] Ren Y, Hao L, Ge Y, Wang X, Tan J. Particulate matter emissions from GDI gasoline engines: Systematic analysis of operating conditions and fuel injection. Fuel 2026;406:136972. https://doi.org/10.1016/j.fuel.2025.136972.

[22] Lou D, Wang T, Fang L, Tan P, Hu Z, Zhang Y, et al. Investigation of the combustion and particle emission characteristics of a GDI engine with a 50 MPa injection system. Fuel 2022;315:123079. https://doi.org/10.1016/j.fuel.2021.123079.

[23] Berg V, Koopmans L, Sjöblom J, Dahlander P. Characterization of gaseous and particle emissions of a direct injection hydrogen engine at various operating conditions. SAE Technical Paper 2023. https://doi.org/10.4271/2023-32-0042.

[24] Denny M, Berntsson A, Helmantel A. The New Aurobay Medium-power Miller Engine. MTZ Worldwide 2024;85:16–23. https://doi.org/10.1007/s38313-024-1971-8.

[25] Yamaguchi A, Dillner J, Helmantel A, Koopmans L, Dahlander P. Ultra-high fuel pressure in GDI to suppress particulate formation during warming-up and load transients. SAE Technical Paper 2023. https://doi.org/10.4271/2023-01-0239.

[26] Gürbüz H, Gülcan HE. Energy, exergy, and exergoeconomic analysis of the use of hydrogen, LPG, and gasoline in an air-cooled SI engine running at stoichiometric conditions. Int J Hydrogen Energy 2025;138:1170–9. https://doi.org/10.1016/j.ijhydene.2025.03.226.

[27] Richter H, Howard JB. Formation of polycyclic aromatic hydrocarbons and their growth to soot—a review of chemical reaction pathways. Prog Energy Combust Sci 2000;26:565–608. https://doi.org/10.1016/S0360-1285(00)00009-5.

[28] Frenklach M, Wang H. Detailed modeling of soot particle nucleation and growth. Symp (Int) Combust 1991;23:1559–66. https://doi.org/10.1016/S0082-0784(06)80426-1.

[29] Agarwal AK, Krishnamoorthi M. Review of morphological and chemical characteristics of particulates from compression ignition engines. Int J Engine Res 2022:146808742211145. https://doi.org/10.1177/14680874221114532.

[30] Drozd GT, Zhao Y, Saliba G, Frodin B, Maddox C, Oliver Chang M-C, et al. Detailed speciation of intermediate volatility and semivolatile organic compound emissions from gasoline vehicles: Effects of cold-starts and implications for secondary organic aerosol formation. Environ Sci Tech 2019;53:1706–14. https://doi.org/10.1021/acs.est.8b05600.

[31] Wang B, Mosbach S, Schmutzhard S, Shuai S, Huang Y, Kraft M. Modelling soot formation from wall films in a gasoline direct injection engine using a detailed population balance model. Appl Energy 2016;163:154–66. https://doi.org/10.1016/j.apenergy.2015.11.011.

[32] Po-i Lee. Combustion visualization and particulate matter emission of a GDI engine by using gasoline and E85. A Thesis, Wayne State University, 2014.

[33] Wang C, Xu H, Herreros JM, Wang J, Cracknell R. Impact of fuel and injection system on particle emissions from a GDI engine. Appl Energy 2014;132:178–91. https://doi.org/10.1016/j.apenergy.2014.06.012.

[34] Sun Z, Cui M, Nour M, Li X, Hung D, Xu M. Differences in pool-fire induced soot production between subcooled spray and flash boiling spray in a DISI engine. Fuel 2021;287:119453. https://doi.org/10.1016/j.fuel.2020.119453.

[35] Singh E, Kim N, Vuilleumier D, Skeen S, Cenker E, Sjöberg M, et al. Particulate matter emissions in gasoline Direct-Injection spark-ignition engines: sources, fuel dependency, and quantities. Fuel 2023;338:127198. https://doi.org/10.1016/j.fuel.2022.127198.

[36] Berndorfer A, Breuer S, Piock W, Von Bacho P. Diffusion combustion phenomena in GDi engines caused by injection process. SAE Technical Paper 2013. https://doi.org/10.4271/2013-01-0261.

[37] Medina M, Alzahrani F, Fatouraie M, Wooldridge M, Sick V. Mechanisms of fuel injector tip wetting and tip drying based on experimental measurements of engine-out particulate emissions from gasoline direct-injection engines. Int J Engine Res 2021;22:2035–53. https://doi.org/10.1177/1468087420916052.

[38] Yamaguchi A, Koopmans L, Helmantel A, Dillner J, Dahlander P. Spray behaviors and gasoline direct injection engine performance using ultrahigh injection pressures up to 1500 bar. SAE International Journal of Engines 2021;15:03-15-01–0007. Doi:10.4271/03-15-01-0007.

[39] Abboud R, Singh E, Lopez-Pintor D, Sjöberg M, Payri R, Javier LJ. Effect of operating conditions on soot-formation pathways in an optical direct-injection gasoline engine. Fuel 2025;385:134173. https://doi.org/10.1016/j.fuel.2024.134173.

[40] Dahlander P, Hemdal S. High-speed photography of stratified combustion in an optical GDI engine for different triple injection strategies. SAE Technical Paper 2015. https://doi.org/10.4271/2015-01-0745.

[41] Smith CM, Hoehler MS. Imaging through fire using narrow-spectrum illumination. Fire Technol 2018;54:1705–23. https://doi.org/10.1007/s10694-018-0756-5.

[42] Etikyala S, Dahlander P. Soot sources in warm-up conditions in a GDI engine. SAE Technical Paper 2021. https://doi.org/10.4271/2021-01-0622.

[43] Hunicz J, Mikulski M, Koszałka G, Ignaciuk P. Detailed analysis of combustion stability in a spark-assisted compression ignition engine under nearly stoichiometric and heavy EGR conditions. Appl Energy 2020;280:115955. https://doi.org/10.1016/j.apenergy.2020.115955.

[44] Zhang Y, Wang Q, Yang R, Yan Y, Fu J, Liu Z. Numerical investigation of the effect of injection timing on the in-cylinder activity of a gasoline direct injection engine. Adv Mech Eng 2022;14:168781322210828. https://doi.org/10.1177/16878132221082873.

[45] Apicella B, Catapano F, Di Iorio S, Magno A, Russo C, Sementa P, et al. Comprehensive analysis on the effect of lube oil on particle emissions through gas exhaust measurement and chemical characterization of condensed exhaust from a DI SI engine fueled with hydrogen. Part 2: effect of operating conditions. Int J Hydrogen Energy 2024;49:968–79. https://doi.org/10.1016/j.ijhydene.2023.09.279.

[46] Qian Y, Wang J, Li Z, Jiang C, He Z, Yu L, et al. Improvement of combustion performance and emissions in a gasoline direct injection (GDI) engine by modulation of fuel volatility. Fuel 2020;268:117369. https://doi.org/10.1016/j.fuel.2020.117369.

[47] Johansson AN, Dahlander P. Experimental investigation on the influence of boost on emissions and combustion in an SGDI-engine operated in stratified mode. SAE Technical Paper 2015. https://doi.org/10.4271/2015-24-2433.

[48] Zhu R, Hu J, Bao X, He L, Zu L. Effects of aromatics, olefins and distillation temperatures (T50 & T90) on particle mass and number emissions from gasoline direct injection (GDI) vehicles. Energy Policy 2017;101:185–93. Doi:10.1016/j.enpol.2016.11.022.

[49] Zhang W, Ma X, Shuai S, Wu K, Macias JR, Shen Y, et al. Effect of gasoline aromatic compositions coupled with single and double injection strategy on GDI engine combustion and emissions. Fuel 2020;278:118308. https://doi.org/10.1016/j.fuel.2020.118308.

[50] Yang J, Roth P, Zhu H, Durbin TD, Karavalakis G. Impacts of gasoline aromatic and ethanol levels on the emissions from GDI vehicles: Part 2. Influence on particulate matter, black carbon, and nanoparticle emissions. Fuel 2019;252:812–20. https://doi.org/10.1016/j.fuel.2019.04.144.

[51] Griffin EA, Gülder ÖL. Soot formation in diluted laminar ethene, propene and 1-butene diffusion flames at elevated pressures. Combust Flame 2018;197:378–88. https://doi.org/10.1016/j.combustflame.2018.08.010.

[52] Xu L, Yan F, Wang Y. A comparative study of the sooting tendencies of various C5–C8 alkanes, alkenes and cycloalkanes in counterflow diffusion flames. Appl Energy Combust Sci 2020;1–4:100007. https://doi.org/10.1016/j.jaecs.2020.100007.

[53] Jain AK, Pathak S, Singh Y, Singh S, Saxena M, Subramanian M, et al. Effect of gasoline composition (Olefins, Aromatics and Benzene) on exhaust mass emissions from two-wheelers - an experimental study. SAE Technical Paper 2007. https://doi.org/10.4271/2007-26-014.

[54] Jiao Q, Reitz RD. The effect of operating parameters on soot emissions in GDI engines. SAE Int J Engines 2015;8:1071. https://doi.org/10.4271/2015-01-1071.

[55] David Kittelson, Markus Kraft. Kittelson, David B. and Markus Kraft. Particle Formation and Models in Internal Combustion Engines. Preprint. University of Cambridge; 2014.

[56] Sirignano M, D'Anna A. Filtration and coagulation efficiency of sub-10 nm combustion-generated particles. Fuel 2018;221:298–302. https://doi.org/10.1016/j.fuel.2018.02.107.

[57] Schurl S, DrS S, DrM B. Impact of 3-way catalytic converters on particulate emission of MPFI motorcycle engines. SAE Technical Paper 2022. https://doi.org/10.4271/2022-32-0004.

[58] Rönn K, Swarts A, Kalaskar V, Alger T, Tripathi R, Keskiväli J, et al. Low-speed pre-ignition and super-knock in boosted spark-ignition engines: a review. Prog Energy Combust Sci 2023;95:101064. https://doi.org/10.1016/j.pecs.2022.101064.

[59] Bikas G, Michos K. Carbon monoxide emissions model for data analytics in internal combustion engine applications derived from post-flame chemical kinetics. SAE International Journal of Engines 2018;11:2018-01–1153. Doi:10.4271/2018-01-1153.

[60] Ling Z, Slaymaker J, Zhou Z, Yang Y, Brear M, Leone TG, et al. Impact of octane numbers on combustion performance and driving cycle fuel consumption of turbocharged direct-injection spark-ignition engine. Fuel 2024;374:132287. https://doi.org/10.1016/j.fuel.2024.132287.